ADVANCING EARTH AND SPACE SCIENCES

JGR Solid Earth

RESEARCH ARTICLE
10.1029/2023JB026536

Stabilizing Effect of High Pore Fluid Pressure on Fault Growth During Drained Deformation

Zachary Zega[1] and Wenlu Zhu[1]

[1]Department of Geology, University of Maryland, College Park, MD, USA

Key Points:

- High pore fluid pressure stabilizes fault propagation in porous sandstone deformed under drained conditions
- Slow faulting was associated with pervasive microcracking and diffuse shear bands only in samples deformed sufficiently slow
- Pervasive subcritical cracking enables slow faulting at high pore fluid pressure under drained conditions at the sample scale

Supporting Information:

Supporting Information may be found in the online version of this article.

Correspondence to:

Z. Zega,
zega@umd.edu

Citation:

Zega, Z., & Zhu, W. (2023). Stabilizing effect of high pore fluid pressure on fault growth during drained deformation. *Journal of Geophysical Research: Solid Earth*, *128*, e2023JB026536. https://doi.org/10.1029/2023JB026536

Received 8 FEB 2023
Accepted 17 JUL 2023

Author Contributions:

Data curation: Zachary Zega
Funding acquisition: Wenlu Zhu
Supervision: Wenlu Zhu
Writing – original draft: Zachary Zega
Writing – review & editing: Wenlu Zhu

Abstract Dilatant hardening is an accepted model for the stabilizing effect of high pore fluid pressure on fault slip and operates when deformation is undrained. To test whether high pore fluid pressure impedes fault propagation under drained conditions, we deformed highly permeable Darley Dale sandstone using strain rates of 10^{-4} s^{-1}, 10^{-5} s^{-1}, and 10^{-6} s^{-1}, respectively. For each strain rate, we compared the inelastic behaviors and faulting styles among rocks deformed under different pore fluid pressures (P_f) (2–180 MPa). The confining pressure (P_c) was attuned to the pore fluid pressure throughout deformation to maintain a constant differential pressure ($P_c - P_f$) of 10 MPa. In samples deformed at 10^{-4} s^{-1} and 10^{-5} s^{-1}, faulting behaviors were similar regardless of the magnitude of pore fluid pressure. However, when the strain rate was lowered to 10^{-6} s^{-1}, we observed prolonged stress drops and slower slip velocities in samples deformed under high pore fluid pressures. In samples deformed at 10^{-6} s^{-1}, we demonstrate that chemically assisted subcritical crack growth played an important role during faulting. A quantitative microstructural analysis revealed that slow faulting at slow strain rates was accompanied by pervasive microcracking and diffuse shear bands, which suggests pervasive subcritical cracking enabled slow faulting under drained conditions at the sample length scale. High pore fluid pressure may have facilitated slow faulting chemically by increasing the rate of subcritical cracking, mechanically via localized dilatant hardening, or both. Our results provide insight into the mechanics of faulting in natural settings where subcritical cracking is prevalent.

Plain Language Summary Sudden, unstable movements of faults produce earthquakes. Slow earthquakes occur when fault motions are unstable but sluggish. Slow earthquakes are often observed in regions where the interstitial fluid pressure within the void space of rocks (pore fluid pressure) is elevated. Dilatant hardening is a well-accepted mechanism that explains why slow earthquakes occur when pore fluid pressures are high. If the rate of fluid transport cannot keep pace with the generation of new void space, the pore fluid pressure drops, and tighter clamping at the propagation front impedes fault motion. We investigate whether slow faulting can also occur when the pore fluid is expected to diffuse quickly within a deforming rock. Permeable sandstone samples were deformed to failure under pressure conditions typical of Earth's uppermost crust at a range of deformation rates. We demonstrate that even when there was ample time for fluid to diffuse throughout the rock sample, high pore fluid pressures can stabilize failure when the rock is deformed at sufficiently slow strain rates. We found that chemical processes play an important role in fracture coalescence at slow loading rates. Enhanced subcritical crack growth can impede fault propagation through combined chemical and mechanical processes at high pore fluid pressure.

1. Introduction

Slow slip events, including non-volcanic tremors (e.g., Obara, 2002), are often collocated with regions of high pore fluid pressure along faults (e.g., Shelly et al., 2006). During a slow slip event, fault movement occurs faster than the average tectonic rate but slower than the slip velocity of typical earthquakes (Peng & Gomberg, 2010). However, the mechanical link between high pore fluid pressure and slow slip remains unclear.

Pore fluid pressure affects fault strength and slip primarily through the effective stress law (e.g., Terzaghi, 1943). The effective stress law states that the effective normal stress (σ_n') *is* equal to the normal stress (σ_n) minus the pore fluid pressure (P_f) multiplied by the effective stress coefficient (α) (i.e., $\sigma_n' = \sigma_n - \alpha P_f$, where $\alpha = 1$ for most rock types) (e.g., In Paterson & Wong, 2005). In the brittle upper crust, fault slip occurs when the shear stress acting on a fault exceeds its shear strength (τ_c), where τ_c is equal to the friction coefficient (μ) times the effective normal stress (σ_n') (i.e., $\tau_c = \mu\sigma_n'$). According to the effective stress law, increasing pore fluid pressure (P_f) lowers the

effective normal stress (σ_n') and reduces the shear strength of the fault (τ_c), which allows fault slip (i.e., failure) at lower levels of shear stress.

In intact rocks, after the shear strength (τ_c) is attained, dilatant microcracking and shear localization result in the formation of a fault. Brittle faulting causes a reduction of load-bearing capacity, which results in a stress drop (Reches & Lockner, 1994). During conventional triaxial compression experiments, dynamic faulting occurs when weakening of the rock occurs at a faster rate than the elastic surroundings. In contrast, quasi-stable faulting occurs when rock weakens at a slower rate than the surroundings (Rice & Rudnicki, 1979; Scholz, 2002). Assuming the stiffness of the surroundings to be constant, a transition from rapid, dynamic faulting to slower, quasi-stable faulting can occur if weakening of the rock occurs at a slower rate.

Rice (1975) proposed that, during brittle faulting, dilatant crack propagation causes the pore fluid pressure at the crack front to drop, hence impeding further crack growth (i.e., hardening) (see also Rice & Rudnicki, 1979; Rudnicki & Chen, 1988). This so-called dilatant hardening is often invoked to explain the stabilizing effect of high pore fluid pressure on slow slip (e.g., Brantut, 2021; Dal Zilio et al., 2020; Liu & Rice, 2007; Rudnicki & Zhan, 2020; Segall et al., 2010). The occurrence of dilatant hardening during deformation hinges on the competition between two timescales: the timescale for fluid diffusion (t_f) and the timescale of deformation (t_d). Long fluid diffusion timescales (t_f) correspond to slow rates of diffusion (v_f) and long timescales for deformation (t_d) correspond to slow deformation rates (v_d).

When $t_f < t_d$ (i.e., $v_f > v_d$), pore fluid readily diffuses, and pore fluid pressure re-equilibrates throughout the deforming rock. In this scenario, the deformation is drained, and the effect of dilatant hardening is negligible. In contrast, when $t_f > t_d$ (i.e., $v_f < v_d$), void space is created at a faster rate than the pore fluid can diffuse to the newly created space. Consequently, the pore fluid pressure drops, and deformation is undrained. Under undrained conditions, locally high effective normal stress encumbers crack growth. This so-called dilatant hardening (Rice, 1975) is responsible for stabilizing both brittle failure (e.g., Aben & Brantut, 2021; French & Zhu, 2017; Martin, 1980) and frictional slip (e.g., Bedford et al., 2021; Lockner & Byerlee, 1994; Xing et al., 2019).

Following Duda and Renner (2013), we will determine the drainage conditions during rock deformation experiments using the macroscopic strain rates and bulk hydraulic properties (see also Bernabe & Brace, 1990; Brace & Martin, 1968; Fischer & Paterson, 1992). The timescale for fluid diffusion, or how quickly fluid diffuses, is equal to the sample length (L) squared divided by the bulk hydraulic diffusivity (D) (i.e., $t_f = L^2/D$), and the timescale for deformation (t_d) is estimated as the amount of time over which significant volume changes are expected to occur during deformation. In this context, when deformation is drained (i.e., $v_f > v_d$ or $t_f < t_d$), the mechanical behavior is primarily controlled by the effective stress (i.e., $\sigma_n' = \sigma_n - \alpha P_f$, where $\alpha = 1$) because pore fluid diffuses more quickly than the sample deforms, and the pore fluid pressure is constant throughout the sample. Conversely, when deformation is undrained (i.e., $v_f < v_d$ or $t_f < t_d$), the pore fluid diffuses slower than the sample deforms, causing the actual pore fluid pressure to differ from the applied P_f. When the sample is undrained, the effective stress is no longer $\sigma_n - P_f$ (i.e., $\sigma_n' = \sigma_n - \alpha P_f$, where $\alpha \neq 1$). Notably, the drainage condition is highly scale dependent. Heterogeneities in mineralogy and pore distribution within a natural rock (e.g., a clay patch within a porous sandstone) can lead to different drainage conditions at different length scales.

In compact rocks (initial porosity <1%) deformed under the same differential pressure (i.e., $P_{dif} = P_c - P_f$), previous experimental studies show that high pore fluid pressures stabilizes fault propagation (e.g., Aben & Brantut, 2021; French & Zhu, 2017; Martin, 1980). Martin (1980), French and Zhu (2017), and Aben and Brantut (2021) all argue that the observed stabilizing effect of high pore fluid pressure on fault propagation was due to dilatant hardening. In these experiments, the deforming samples likely became undrained post-failure due to low bulk permeabilities of compact rocks; fluid diffused relatively slowly from the surroundings into the more rapidly propagating fault (i.e., $v_f < v_d$ or $t_f > t_d$), and dilatant hardening stabilized faulting.

It is unclear whether high pore fluid pressure can stabilize faulting in more permeable, dilatant rocks such as porous sandstones. This is because the deformation of porous sandstones is expected to be drained over a wide range of laboratory strain rates. If dilatant hardening is the sole mechanism responsible for slow faulting under conditions of high pore fluid pressure, then slow faulting is not expected in porous sandstones. However, if the stabilizing effect of high pore fluid pressure is observed in porous sandstones, mechanisms other than dilatant hardening must be investigated.

Relative to compact rocks, porous rocks are generally more susceptible to brittle creep (e.g., Brantut et al., 2013; Heap et al., 2009). Brittle creep, or the time-dependent deformation of brittle rocks, is thought to occur due to subcritical crack growth, which refers to crack growth that occurs at a level of stress below a critical

Table 1
Summary of Experiments

Sample ID	Porosity, %	Confining pressure (P_c), MPa	Pore fluid pressure (P_f), MPa	Strain rate ($\dot{\varepsilon}$), s^{-1}	Differential pressure ($P_{dif} = P_c - P_f$), MPa
D10-4-1	15.0	20	10	10^{-4}	10
D120-4-1	14.3	130	120	10^{-4}	10
D2-5-1	14.7	12	2	10^{-5}	10
D120-5-1	14.8	130	120	10^{-5}	10
D180-5-1	15.3	190	180	10^{-5}	10
D2-6-1	15.2	12	2	10^{-6}	10
D10-6-1	14.7	20	10	10^{-6}	10
D120-6-1	15.6	130	120	10^{-6}	10
D180-6-1	15.0	190	180	10^{-6}	10
D10-4-2[a]	13.8	20	10	10^{-4}	10
D120-4-2[a]	15.2	130	120	10^{-4}	10
D2-5-2[a]	15.3	12	2	10^{-5}	10
D120-5-2[a]	14.7	130	120	10^{-5}	10
D2-6-2[a]	12.8	12	2	10^{-6}	10
D10-6-2[a]	13.5	20	10	10^{-6}	10
D120-6-2[a]	13.1	130	120	10^{-6}	10
D180-6-2[a]	12.6	190	180	10^{-6}	10

[a]Experimental data shown in Supporting Information S1.

value required for dynamic crack growth (e.g., Atkinson, 1984). Under upper-crustal conditions, subcritical cracking is thought to be primarily driven by water-assisted stress corrosion reactions that break silicate bonds and allow for time-dependent deformation and the eventual failure of rock placed under a constant stress (e.g., Anderson & Grew, 1977; Martin & Durham, 1975; Scholz, 1972). In contrast to subcritical crack growth, cracks also grow in a time-independent manner due to the stress transfer when the stress at a crack tip exceeds a threshold value. In general, time-independent cracking due to stress transfer is the dominant process in rocks deformed at fast strain rates; however, at increasingly slow strain rates, more time is allowed for stress corrosion reactions to facilitate subcritical crack growth (e.g., Sano et al., 1981).

The contrast in mechanical behaviors observed in wet versus dry rocks due to subcritical cracking has already been extensively documented (e.g., Baud et al., 2000; Duda & Renner, 2013; Hadizadeh & Law, 1991), but exactly how the magnitude of pore fluid pressure affects subcritical cracking remains less clear. Conditions of high pore fluid pressure may alter the rate of subcritical crack growth by changing the chemical activity of reactants associated with stress corrosion or by supplying additional reactants to crack tips (e.g., Atkinson & Meredith, 1981; Fyfe, 1978; Heap et al., 2009). Furthermore, whether the hydraulic properties of a subcritical crack differ from those of a time-independent crack is currently unknown. It is conceivable that dilatant hardening can significantly impact the growth and coalescence of subcritical cracks.

To investigate the effect of high pore fluid pressure on fault slip during drained deformation, we deformed 17 water-saturated samples of highly permeable Darley Dale sandstone using strain rates of 10^{-4} s^{-1}, 10^{-5} s^{-1}, and 10^{-6} s^{-1}. At each strain rate, we compared the deformation behaviors and faulting style among rocks deformed under different pore fluid pressures ranging from 2 to 180 MPa. In total, four experiments were completed at the fastest strain rate, five experiments were completed at the intermediate strain rate, and eight experiments at the slowest strain rate (Table 1). We adopted the same experimental protocol as in French and Zhu (2017): In all experiments, the confining pressure (P_c) was attuned to the pore fluid pressure (P_f) to maintain a constant differential pressure of 10 MPa (i.e., $P_{dif} = P_c - P_f = 10$ MPa) throughout the entirety of deformation. Quantitative microstructural analyses of samples deformed at different conditions were conducted. A damage map was produced to show the spatial distribution of damage in samples deformed under varying conditions. A comparison of crack densities was made among samples deformed at different strain rates and pore fluid pressures. Based on these observations, we propose new mechanisms that are potentially responsible for slow faulting under drained conditions in porous rocks deformed under high pore fluid pressures.

2. Methodology

2.1. Porous Sandstone Samples

Rock deformation experiments and microstructural analyses were performed on samples of Darley Dale sandstone deformed using a constant differential pressure of 10 MPa, strain rates ranging from 10^{-4} s^{-1} to 10^{-6} s^{-1}, and pore fluid pressures ranging from 2 to 180 MPa (Figure 1; Table 1). This rock was chosen because its mechanical and transport properties are well characterized (e.g., Brantut et al., 2013; Heap et al., 2009; Wong et al., 1997; Zhu & Wong, 1997). With permeability ranging from 10^{-13} m^2 to 10^{-14} m^2, drained conditions can be achieved in this rock deformed at the pressures and strain rates used in this study (Table 1). Heap et al. (2009) reported a modal composition for Darley Dale of 69% quartz, 26% feldspar, 3% clays, and 2% mica and measured grain sizes between 0.1 and 0.8 mm. For samples used in this study, the measured initial porosity varied between 12.6% and 15.6% (Table 1). Experiments labeled with the number "1" at the end of the sample ID are summarized in the main text while experiments labeled with the number "2" at the end of the sample ID are outlined in Supporting Information S1 (Table 1).

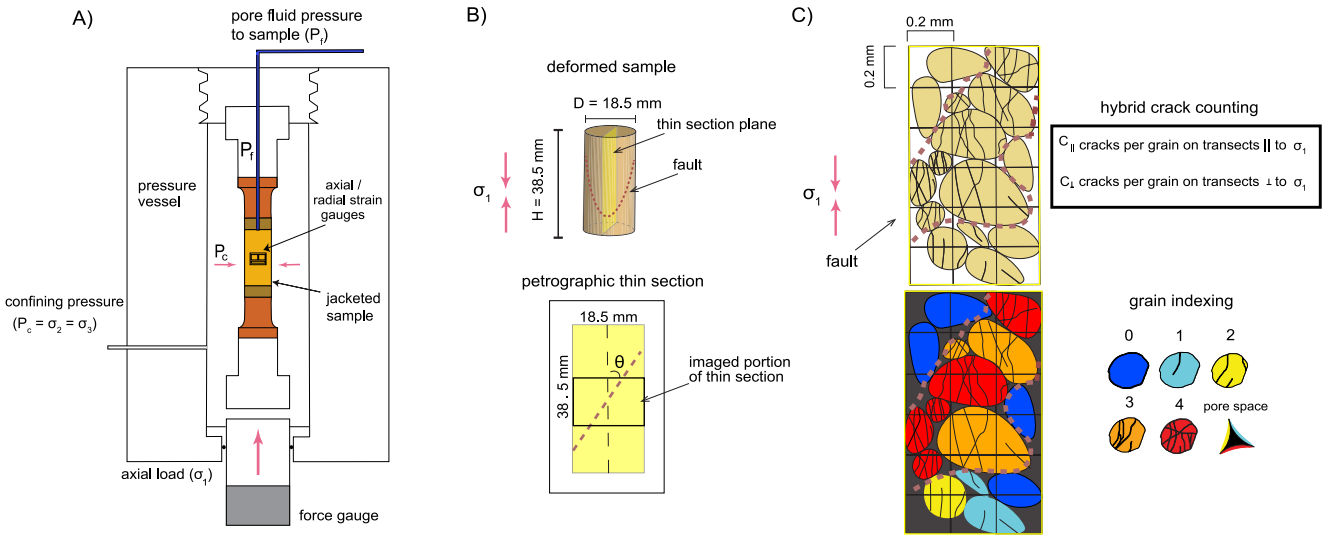

Figure 1. (a) Schematic of the loading configuration used to deform Darley Dale sandstone. (b) Deformed samples were cut at an orientation to maximize the area of the fault observed in thin section, and photomicrographs were mosaiced together to create large images of the middle third of the sample. (c) Various crack counting techniques and grain indexing methods were employed to quantify crack density, fault morphology and fracture patterns for certain deformed samples. 0.2 mm approximates the mean intercept length of grains observed in thin section.

2.2. Sample Preparation

All samples of Darley Dale sandstone were cored perpendicular to bedding from the same block. Each sample was cut and ground into a right cylinder with a diameter of 18.41 mm (0.725 in.) and a length of 38.10 mm (1.5 in.) or with a diameter of 25.40 mm (1 in.) and a length of 50.80 mm (2 in.). All sample lengths and diameters were measured in triplicate to ensure that samples were consistently cut to the correct size. Samples were dried in a heated vacuum oven for 24 hr at 60˚C. Once dried, each sample was weighed on an analytical balance three separate times to obtain an average mass. Once the average dry mass was obtained, samples were exposed to water vapor under vacuum and then saturated in deionized water for 24 hr. After the saturation period, the average saturated mass was determined by weighing the sample three separate times. To calculate initial porosity of a given sample, the pore volume was estimated by taking the difference between the average dry and average saturated mass and dividing it by the density of deionized water. Porosity is the ratio between the pore volume and the total sample volume calculated using the measured dimensions of the sample. Samples were kept in deionized water prior to an experiment for no more than 3 days.

Preceding an experiment, a sample was tightly wrapped with a copper foil with a thickness of 0.05 mm. To collapse the copper jacket onto the sample, the sample was placed into a pressure vessel, and a pneumatic Haskel pump (air-driven booster) was used to pump kerosene into the vessel to apply ~7 MPa confining pressure to the sample. Once the jacket was fitted, a small section of the jacket was sanded with sandpaper and cleaned with isopropyl alcohol to allow axial and radial strain gauges to be securely glued to the surface of the copper. The copper-jacketed sample with strain gauges was placed between two double O-ring endcaps and a series of spacers that were attached to a base plug that seals one end of the pressure vessel in a triaxial deformation apparatus (Figure 1). The sample was held in place with polyolefin heat-shrink tubing and hand-twisted 24-gauge steel wires. Holes were added to the polyolefin to allow wires coming from the strain gauge to be attached to the base plug. These holes were later sealed with a room-temperature vulcanizing silicone gel before an experiment.

2.3. Constant Strain Rate Deformation Experiments

The triaxial deformation apparatus used in this study allowed for independent servo control of confining pressure (P_c), axial stress (σ_1), and pore fluid pressure (P_f) (e.g., Ougier-Simonin & Zhu, 2015). P_c is first introduced using a booster pump and is then servo controlled using an intensifier. P_f is first introduced to the sample by filling an intensifier with deionized water using a hand pump. The P_f is controlled using an intensifier that applies pressure through a hollow series of spacers that lead to the sample (Figure 1). The deformation apparatus is in a climate-controlled room where the temperature is maintained at 23˚C.

Kerosene was used as the confining medium and deionized water was used as the pore fluid. A main ram controlled by hydraulics was used to apply an axial load to the sample during an experiment. For the experiments in this study, the ram was moved at constant displacement rates that result in constant axial strain rates of 10^{-4} s^{-1}, 10^{-5} s^{-1}, or 10^{-6} s^{-1}, respectively. Values of P_c and P_f were recorded during an experiment by using pressure transducers located outside of the pressure vessel. Axial stress (σ_1) was measured by a force gauge that was placed outside of the pressure vessel and was corrected for seal friction, which was measured prior to axial deformation of the sample. Axial strain was measured at the sample with an axial strain gauge that was attached to the copper jacket that surrounded the sample. Additionally, axial strain was deduced from a linear variable differential transducer (LVDT) that measures the displacement of the main ram by correcting the measured displacement data for the stiffness of the deformation apparatus (determined to be 208 kN/mm). All mechanical data in this study are plotted using axial strain inferred from the LVDT corrected for rig stiffness. Volumetric strain (ε_v) was calculated using axial strain (ε_a) measurements and radial strain (ε_r) measured by the radial strain gauge on the copper jacket (i.e., $\varepsilon_v = \varepsilon_a + 2\varepsilon_r$; Brace et al., 1966). All data were recorded at a frequency of 2 Hz. The experimental conditions used in this study are listed in Table 1. Experiments included in Supporting Information S1 are meant to demonstrate the reproducibility of experiments shown in the main text. A high level of reproducibility is shown at all strain rates.

In each experiment, a confining pressure of ~7 MPa was first applied to the sample. Then, a pore fluid pressure of ~4 MPa was applied using a hand pump. Samples deformed at P_c = 12 MPa and P_f = 2 MPa were left to pre-compact for 1 hour after adjusting the pressures to P_c = 12 MPa and P_f = 2 MPa. For experiments performed at higher pressures, the sample was pre-compacted for 1 hr at P_c = 20 MPa and P_f = 10 MPa. Following pre-compaction, both P_c and P_f were increased at a constant rate while maintaining a constant differential pressure ($P_{dif} = P_c - P_f$) of 10 MPa. Once the pre-determined pressure conditions were reached, the radial stresses ($\sigma_2 = \sigma_3 = P_c$) and the pore fluid pressure P_f were kept constant via servocontrol throughout the deformation test.

In each experiment, after peak stress was reached and the subsequent stress drop leveled off, the hydraulic ram was moved away from the sample to stop axial deformation. All experiments were accompanied by inaudible stress drops, and different rates of weakening were observed. The deformed samples were unloaded at a constant differential pressure of 10 MPa using the same rate as the initial pressurization to preserve deformation microstructures.

2.4. Thin Section Preparation and Microstructural Analysis

Visual examination of deformed samples retrieved from the pressure vessel revealed that a through-going fracture (i.e., fault) developed in all samples. These samples were dried and impregnated with low-viscosity, slow-curing epoxy. Each sample was then cut in half lengthwise at an orientation that maximized the intersection to the fault plane resulting from the brittle failure (Figure 1b). Using one half of the deformed sample, double polished thin sections (30 μm thick) were made for the microstructural analysis. A grid of test lines was overlaid onto photomicrographs, and the mean intercept length, which represents the average length of a line segment intersecting a large number of grains, was obtained by dividing the length of the test lines by the number of intersections with grains (Underwood, 1969). The average grain size determined using this chord length analysis method was 0.19 mm in sample D180-6-1 (Table 1), which agrees with values reported in other studies (e.g., Wong et al., 1997). Crack counting and grain indexing methods were performed on the middle third of thin sections and are located farthest from the piston and the series of spacers present at the sample edges.

To characterize the fracture patterns of each sample, a grain indexing method first developed by Menéndez et al. (1996) and later adopted by Tamarkin et al. (2012) was used. This grain indexing method was used on large photomosaics that are comprised of images taken at a total magnification of 50× under normal reflected light. A grid of evenly spaced lines was drawn over the photomosaic in Adobe Photoshop to create individual squares that were 0.1 mm × 0.1 mm (roughly one half of the mean intercept length). Boxes with most of their total area falling into pore space were colored black. Grains within boxes were categorized as a "0" and colored blue if no cracks could be seen in the image. Grains were categorized as a "1" and colored cyan if there were only one or two intragranular cracks (defined as cracks that have not propagated across the entire grain). A yellow-colored grain categorized as a "2" indicated a grain with no more than two transgranular cracks (defined as cracks that have propagated diametrically from one side of the grain to the other). Grains were categorized as a "3" and colored orange if there were more than two transgranular cracks, and the grain remained intact. Finally, red grains

categorized as a "4" represent crushed grains (i.e., grains clearly broken into multiple smaller pieces). Unlike grains placed into the "3" category, grains indexed as a "4" were often accompanied by finely crushed debris due to the crushing of the grain.

To compare the intensity of microcracking produced under different pressures and strain rates in a more quantitative manner, we developed a hybrid crack counting method. A grid was placed over photomosaics to create square boxes that were 0.2 mm × 0.2 mm. The 0.2 mm length is roughly equal to the mean intercept length (Figure 1c). The number of cracks encountered per grain along a given transect line was recorded. Cracks per grain counted on transects oriented parallel to σ_1 were labeled $C_{||}$. Cracks per grain counted on transects oriented perpendicular to σ_1 were labeled $C_{\perp}$. The results from the hybrid counting method are semiquantitative since any given transect is recorded as crossing exactly 0, 1, 2, or 3 cracks per grain that the transect crossed in the image. However, if a transect line directly intersected four or more cracks within one grain, then the grain was categorized as having ≥4 cracks. More than 500 grains were counted in each photomosaic.

To quantify the difference in fault width seen in experiments D2-6-1 ($P_f = 2$ MPa) and D180-6-1 ($P_f = 180$ MPa) completed at 10^{-6} s^{-1} (Table 1), three 11 × 11 grids of 0.2 mm × 0.2 mm boxes were placed on top of photomosaics to perform a crack counting routine (Zega & Zhu, 2023). The rectangular grid that was overlaid on both photomosaics contained columns of 11 boxes oriented parallel to the fault. The center column of the grid was placed along the center of the fault zone, as determined from the damage maps created for both samples. The number of cracks present in each box was recorded. Since the columns of boxes in the grid are oriented parallel to the fault plane, the 11 measurements of cracks per box in one column represent 11 individual measurements of crack density that are the same distance from the center of the fault. This process was done iteratively by counting cracks per box in each column from one side of the fault to the opposite side of the fault. This scheme allowed crack densities to be plotted as a function of distance from the core of the fault.

3. Results

3.1. Mechanical Data

In the presentation of these mechanical data, we adopt the convention that positive stresses and strains are compressive. The stress-strain curves in all experiments show 4 typical stages of deformation behavior (Figures 2a, 2d, 2g; Figure S1 in Supporting Information S1): (a) A brief non-linear compaction resulting from the initial crack closure; (b) A quasi-elastic compaction with an approximately linear stress-strain relationship; (c) The onset of shear-induced dilatancy (*C'*) when the stress-strain curve deviated from the initially linear stress-strain relationship; and (d) A strain softening stage after reaching the peak differential stress ($\Delta\sigma_{max}$) when a through-going fault develops. The failure behaviors were not audible in any experiments shown in this work. Instead, all samples displayed varying rates of strain weakening in a quasi-static manner, as shown by the different slopes of the shear stress against time after peak stress plots (Figure 2).

At the same strain rate, the peak stresses of all samples were similar irrespective of the different pore fluid pressures used (Figure 2a, 2d, 2g; Table 2). This suggests that the shear strength depended solely on the differential pressure (constant) and did not vary as a function of the pore fluid pressure, which is in good agreement with the effective stress law with $\alpha = 1$. However, the peak stresses change when samples were deformed using different strain rates. The peak stresses obtained at 10^{-4} s^{-1} are ~10 MPa higher than those deformed at 10^{-5} s^{-1}. The differences in the peak stresses at 10^{-5} s^{-1} and 10^{-6} s^{-1} are within the typical range in peak stresses observed due to sample-to-sample variations. $\Delta\sigma_{max}$ varies by only 1–2 MPa in samples deformed at 10^{-4} s^{-1} and 10^{-5} s^{-1}. Overall, the observed increase in peak stress that was associated with increasing the strain rate from 10^{-5} s^{-1} to 10^{-4} s^{-1} is greater than the variation in peak stress expected due to sample-to-sample variability. In samples deformed at 10^{-6} s^{-1}, the peak stress ranges from 81 to 87 MPa with the exception of one sample (D120-6-2) having a peak stress of 90 MPa. Considering D120-6-2 also has anomalously Young's modulus and *C'* (Table 2), this is likely due to the variability of natural samples. It is interesting to note that the peak stress and Young's modulus of sample D-120-6-2 deformed at 10^{-6} s^{-1} were closer to the values obtained in samples deformed at 10^{-4} s^{-1} (Table 2).

The different slopes of the Stage IV (after the peak stress was attained, thus called post-failure) stress-strain curves signify different rates of fault growth, which can be better visualized by plotting shear stress and slip against time. Inelastic axial strain was deduced using the elastic moduli shown in Table 1, and a trigonometric relationship was used to infer displacement of the fault plane (e.g., Ougier-Simonin & Zhu, 2015). To calculate slip velocity, the derivative of the relative fault displacement with respect to time was plotted to show any accelerations in the

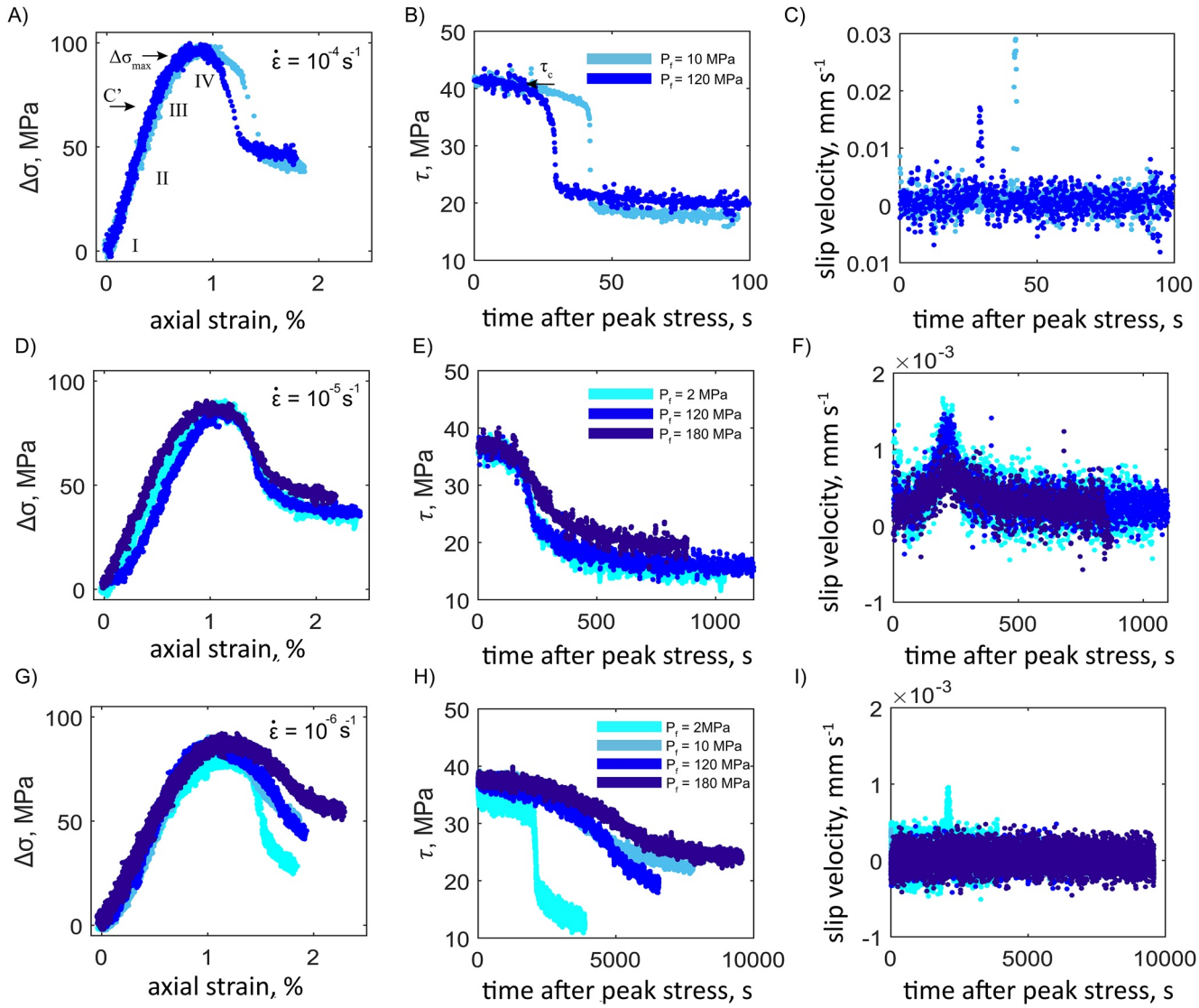

Figure 2. (a, d, g) Stress-strain curves from experiments outlined in Tables 1 and 2. Each color represented a separate experiment. (b, e, h) Shear stress plotted against time after peak stress. (c, f, i) Slip velocity plotted against time after peak stress. (c) has a different *y*-axis than (f) and (i).

slip beyond the imposed loading rate (see Supporting Information S1 for details; Figure 2). Any "spikes" seen in Figures 2c, 2f, or Figure 2i represent accelerations in slip velocity beyond the constant axial displacement rate imposed by the machine. A 30° fault plane was chosen in calculations since the microstructural analysis revealed that a localized zone of damage formed at ~30°±2° from the maximum principal stress (Figure 3; Figure 4; Figure 6). Notably, altering the faulting angle does not significantly change the trends observed in the data. Small variations in the faulting angle (±2°) neither significantly change the calculated values of shear stress or slip velocity, nor do they affect the trends observed in the data (see Supporting Information S1).

At a strain rate of 10^{-4} s^{-1}, samples showed weakening durations (i.e., the time elapsed from $\Delta\sigma_{max}$ to the residual stress measured at the end of axial deformation) of <50 s (Figure 2b). Prior to a rapid stress drop and increase in slip velocity, the stress dropped slowly for ~30 s at $P_f = 120$ MPa and ~40 s at $P_f = 10$ MPa. The abrupt accelerations in slip velocity coincided with abrupt shear stress drops. Qualitatively, the post-peak stress behavior is similar at this strain rate regardless of the pore fluid pressure.

At a strain rate of 10^{-5} s^{-1}, all experiments resulted in a weakening duration of <800 s (Figure 2e). Compared to the experiments completed at 10^{-4} s^{-1}, experiments at 10^{-5} s^{-1} resulted in longer weakening durations and less abrupt shear stress drops but still resulted in measurable accelerations in slip velocity beyond the imposed loading

Table 2
Experimental Data

Sample ID	Confining pressure (P_c), MPa	Pore fluid pressure (P_f), MPa	Strain rate ($\dot{\varepsilon}$), s^{-1}	Young's modulus, GPa[a]	C', MPa[b]	Peak differential stress, MPa
D10-4-1	20	10	10^{-4}	14.8	29	96
D120-4-1	130	120	10^{-4}	14.9	34	95
D2-5-1	12	2	10^{-5}	10.7	29	85
D120-5-1	130	120	10^{-5}	11.4	36	84
D180-5-1	190	180	10^{-5}	11.2	54	86
D2-6-1	12	2	10^{-6}	9.8	24	81
D10-6-1	20	10	10^{-6}	11.7	20	87
D120-6-1	130	120	10^{-6}	11.3	26	86
D180-6-1	190	180	10^{-6}	10.1	-	87
D10-4-2[c]	20	10	10^{-4}	14.7	-	95
D120-4-2[c]	130	120	10^{-4}	10.8	-	96
D2-5-2[c]	12	2	10^{-5}	11.3	-	88
D120-5-2[c]	130	120	10^{-5}	13.1	-	84
D2-6-2[c]	12	2	10^{-6}	11.5	19	81
D10-6-2[c]	20	10	10^{-6}	11.4	23	87
D120-6-2[c]	130	120	10^{-6}	12.5	48	90
D180-6-2[c]	190	180	10^{-6}	11.6	19	84

[a]The Young's modulus was inferred from axial displacement measurements from an LVDT that were corrected for rig stiffness. [b]C' was reported when strain gauge data were available (see Supporting Information S1). [c]Experimental data shown in Supporting Information S1.

rate. In each experiment, the stress initially dropped slowly for a period of ~200 s prior to an acceleration in strain rate (Figure 2f). The measured peaks in slip velocity correspond to the time when samples began to experience a more rapid shear stress drop (Figure 2e). Overall, experiments at a strain rate of 10^{-5} s^{-1} showed a high degree of repeatability and negligible variations in the style of weakening behavior.

All samples deformed at a strain rate of 10^{-6} s^{-1} showed longer weakening durations than experiments completed at the same pressure conditions at higher strain rates. The experiments completed at a strain rate of 10^{-6} s^{-1} also showed the most variety in faulting behaviors. In all experiments at this strain rate, a particularly prolonged drop in the stress of at least 1,000 s was recorded after the sample reached peak differential stress. Unlike experiments completed at the higher strain rates, slip velocity in 5 of the 8 experiments completed at 10^{-6} s^{-1} remained close to the imposed loading rate, which resulted in no visible spike in the slip velocity data as the stress dropped (Figure 2i; Figure S1 in Supporting Information S1). Due to the variety in faulting behaviors, the stress drop occurred rapidly when there was detectable slip acceleration and occurred in a gentle fashion over a longer period for the cases in which the slip velocity remained near the loading rate. Increasing the pore fluid pressure had the most apparent effect on slip behavior at a strain rate of 10^{-6} s^{-1}. Although both fast and slow failure were observed at low P_f (see Figure S1 in Supporting Information S1), the slowest faulting behaviors were more consistently observed at conditions of high pore fluid pressure ($P_f \geq 120$ MPa). Fast faulting was not observed at $P_f = 180$ MPa at a strain rate of 10^{-6} s^{-1}.

3.2. Microstructural Analysis

3.2.1. Spatial Distribution of Damage

Using a grain indexing method outlined in the methods section, we produced damage maps to characterize the fracture patterns in samples deformed under different pressure conditions at two strain rates (Figures 3 and 4). In the two microstructures examined at a strain rate of 10^{-5} s^{-1}, the fracture patterns are qualitatively similar: Damage is localized in a band oriented ~30° from σ_1, and only a few grains away from what one may interpret as the main "fault zone" were categorized as a 4 (Figure 3). In samples deformed at 10^{-5} s^{-1}, increasing the imposed pore fluid pressure had only negligible effects on the observed deformation microstructures.

At a strain rate of 10^{-6} s^{-1}, increasing the pore fluid pressure had a more noticeable effect on the spatial distribution of damage observed in thin section. Unlike those samples deformed at 10^{-5} s^{-1}, the sample deformed at high pore fluid pressure with the slowest faulting behavior (sample D180-6-1) exhibited enhanced off-fault damage and a wider overall damage zone when compared to a sample deformed at low pore fluid pressure with comparatively faster faulting behavior (sample D2-6-1) (Figure 4). At a strain rate of 10^{-6} s^{-1}, slow faulting observed at high pore fluid pressure resulted in both a wider fault and more off-fault damage while faster faulting at lower pore fluid pressure resulted in more localized deformation as observed at the faster strain rate.

To quantify the intensity of microcracking, we applied the hybrid crack counting method and have summarized the results of the counting process in a series of pie charts (Figure 5). These pie charts demonstrate that decreasing the strain rate and increasing the pore fluid pressure resulted in a microstructure with a higher proportion of grains with at least 4 cracks as counted along transects oriented both parallel and perpendicular to the maximum principal stress. At a strain rate of 10^{-6} s^{-1}, increasing pore fluid pressure from 2 to 180 MPa resulted in a 5.7% increase in the total number of grains along horizontal transects (labeled as $C_\perp$) that were determined to have at least four cracks (Figure 5). At the faster strain rate, increasing pore fluid pressure resulted in a 2.5% increase in grains with at least 4 cracks that were sampled along transects in the same orientation (Figure 5). At a strain rate of 10^{-6} s^{-1}, we also measured a 4.8% increase in the number of grains with at least four cracks counted along

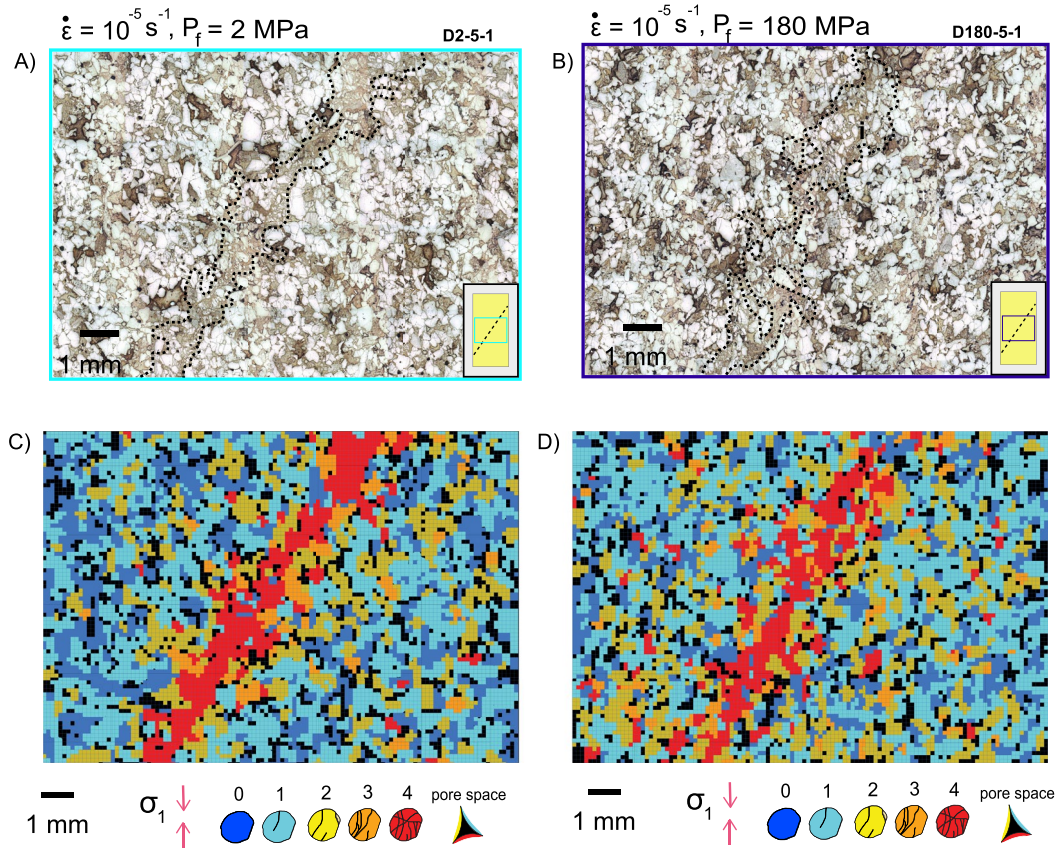

Figure 3. (a),(b) Photomicrographs taken at 50× total magnification under reflected light for experiments D2-5-1 and D180-5-1. The fault is traced in a dotted black line according to the damage maps. The inset thin section graphic shows the imaged area of the thin section for perspective. (c), (d) Associated maps depicting the spatial distribution of damage seen in the photos.

transects oriented parallel to the maximum principal stress (labeled as $C_{||}$) when pore fluid pressure increased from 2 to 180 MPa (Figure 5). In the case of the faster strain rate, increasing pore fluid pressure yielded a 0.2% increase for cracks counted per grain along transects oriented parallel to the maximum principal stress.

3.2.2. Fault Morphology

To discern changes in the width of the fault zone for the experiments completed at low and high P_f (depicted in Figure 4), we used a counting scheme to quantify damage as a function of distance from the fault core in two samples deformed using a strain rate of 10^{-6} s^{-1}. The fault cores were in a similar region of both thin sections and the center point of each fault was chosen by examining the damage maps (see boxed regions in Figures 4a and 4b). In both samples, the highest crack densities sampled were located near the fault core. In the sample deformed at low pore fluid pressure, the median crack density decays sharply with only a small distance from the fault core. However, at high pore fluid pressure, higher crack densities persist some distance from the center of the fault. To the left of the fault core in the negative direction, high median crack densities (>4 cracks per box) were sampled consecutively to −0.8 mm from the center of the fault in the sample deformed at high pore fluid pressure. To the right of the fault core in the positive direction, high median crack densities were sampled consecutively to +1.2 mm from the center of the fault. In contrast, at low pore fluid pressure, the region of continuous high median crack densities extends from −0.6 to +0.6 mm with respect to the center of the fault (Figure 6c). In this region of the sample, the zone of highest crack density is roughly 0.8 mm wider in the sample deformed at high pore fluid pressure. The counting technique reflects what is qualitatively observed in the damage maps and outlined in photomicrographs (Figures 4, and 6a 6a and 6b).

3.2.3. Off-Fault Damage

As observed in the damage maps, a higher number of grains indexed as a 4 were found away from what one may interpret to be the primary fault zone when slow faulting was observed at high pore fluid pressure at the slow

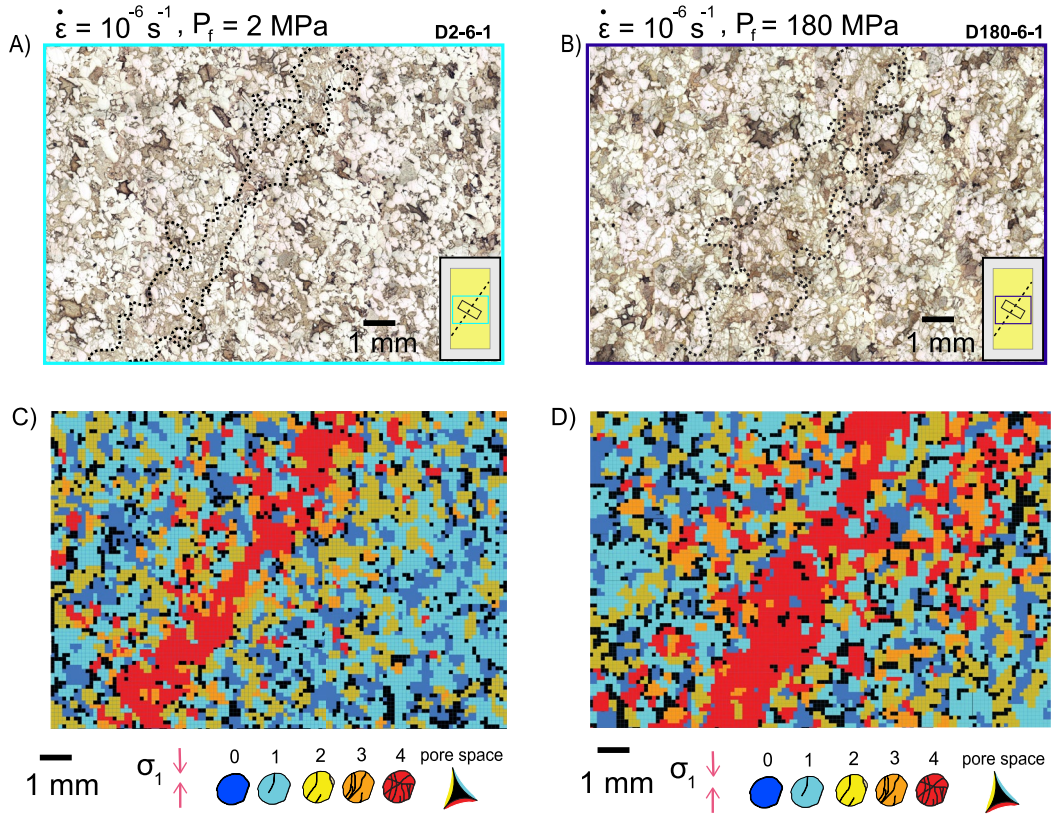

Figure 4. (a), (b) Photomicrographs taken at 50× total magnification under reflected light for experiments D2-6-1 and D180-6-1. The fault is traced in a dotted black line according to the damage maps. The inset thin section graphic shows the imaged area of the thin section for perspective. The black box shows the imaged area seen in Figure 6. (c), (d) Associated maps depicting the spatial distribution of damage seen in the photos.

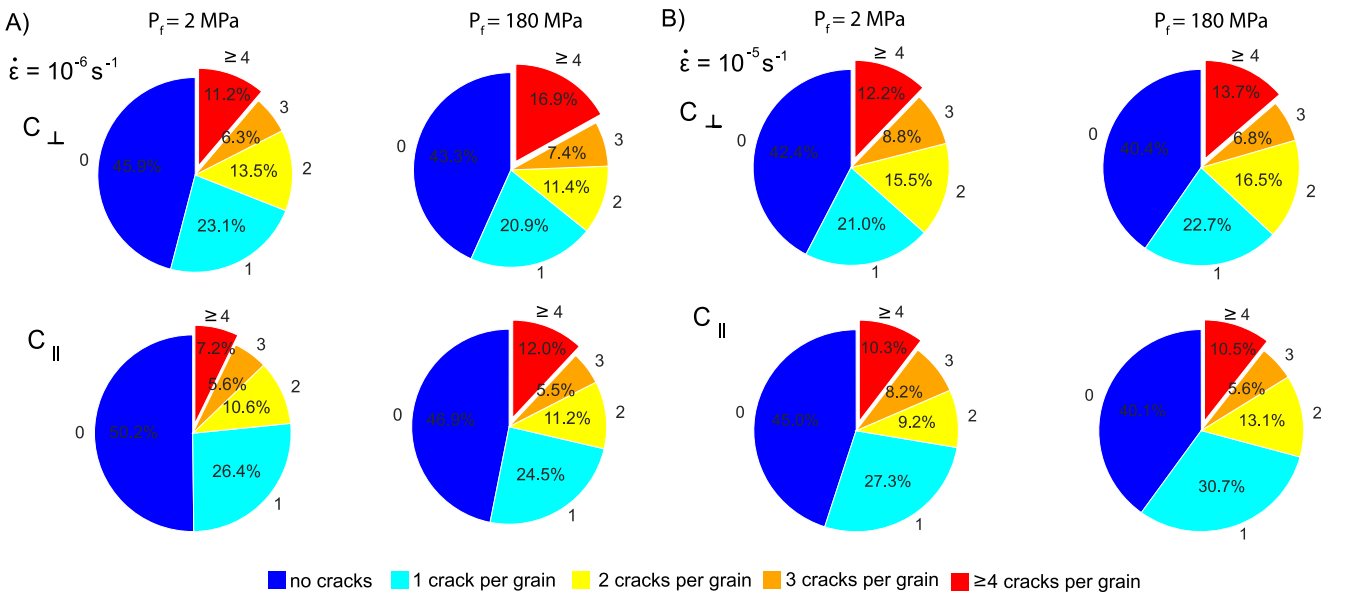

Figure 5. Hybrid crack counting results shown in pie charts for the samples depicted in Figures 3 and 4. (a) Shows the cracks per grain counted on transects both perpendicular (top row) and parallel (bottom row) to the maximum principal stress for experiments D2-6-1 and D180-6-1. (b) Shows the cracks per grain counted both perpendicular (top row) and parallel (bottom row) from the maximum principal stress for experiments D2-6-1 and D180-6-1.

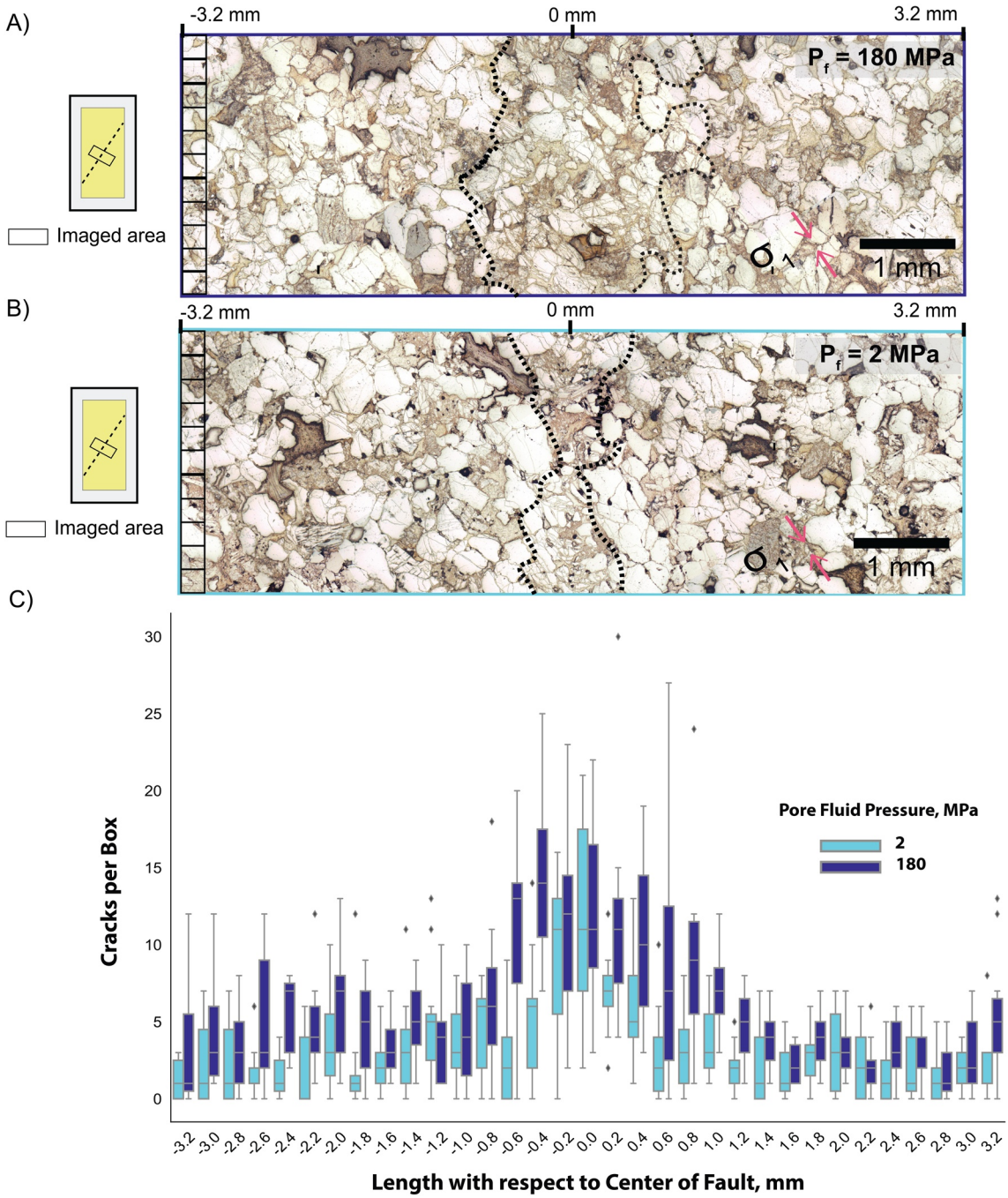

Figure 6. (a), (b) Photomicrographs perpendicular to the fault in samples D180-6-1 and D2-6-1 deformed at 10^{-6} s^{-1}. The fault is traced in a dotted black line according to the damage maps. Inset thin section graphic outlines the imaged area for perspective. The black box in the upper left-hand corner of A and B is 0.2 mm × 0.2 mm and represents the size of the sampling area. (c) A box-and-whisker showing the distribution of cracks per box for each photomicrograph. The colored box displays the interquartile range. The upper and lower bounds (tops and bottoms of the whiskers) are the upper quartile plus 1.5× the interquartile range and the lower quartile minus 1.5× the interquartile range. Points outside of the upper and lower bounds are outliers (black diamonds).

strain rate (Figure 4). To further document the nature of this off-fault damage under conditions of slow faulting, photomicrographs from the experiment completed at $P_f = 120$ and at a strain rate of 10^{-6} s^{-1} (included in Figure 2) were taken at a variety of magnifications under reflected light (Figure 7). Compared to the sample deformed at the lowest pore fluid pressure at the same strain rate ($P_f = 2$ MPa), the sample deformed at $P_f = 120$ MPa experienced markedly slower failure (Figure 2). The same microstructural analysis involving grain indexing and hybrid

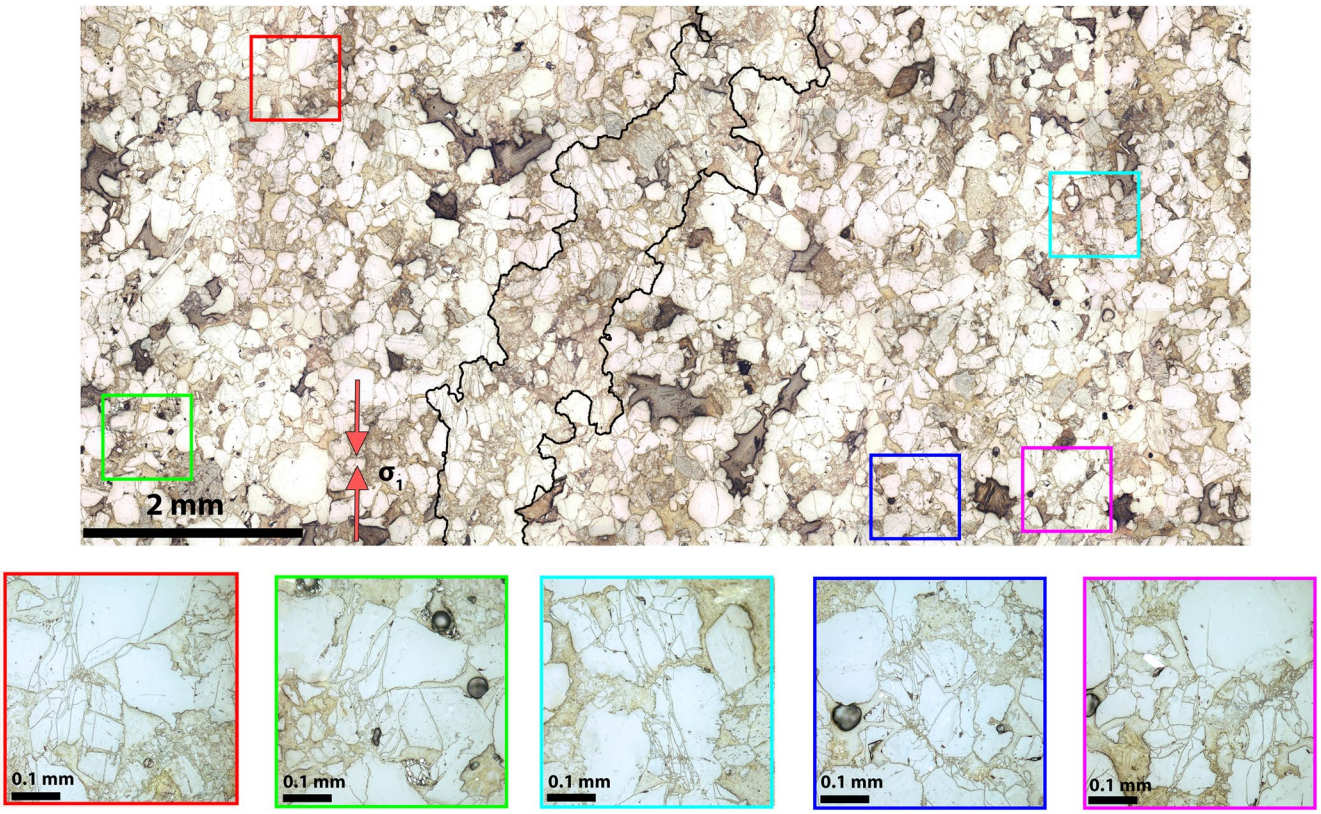

Figure 7. Photomicrographs showing five instances of off-fault damage in sample D120-6-1. The boxed 200× magnification photos match the location of the correspondingly colored box drawn on the larger photomosaic. The black outline on the large photo shows the fault trace as interpreted from the damage map completed on a larger photomosaic.

crack counting was also applied to this sample (see Supporting Information S1). The results demonstrate that there is a higher overall crack density in this experiment compared to the sample deformed at low pore fluid pressure at the same strain rate ($P_f = 2$ MPa at 10^{-6} s^{-1}). The zones of damage shown were indexed as four in the grain indexing scheme, and the outline of the fault was traced according to the damage map (see Figure S2 in Supporting Information S1). Zones of off-fault damage were observed up to 5 mm from the edge of the fault and are seen in the middle third of the thin section. The observed zones of off-fault damage are representative of the style of off-fault damage that appears to be most pervasive at $P_f = 180$ MPa and at a strain rate of 10^{-6} s^{-1}, as indicated in the damage map (Figure 4b).

The first instance of off-fault damage (labeled as 1 in Figure 7) shows an array of intragranular cracks that emanate from a grain contact. So-called hertzian fractures (e.g., Zhang et al., 1990) of this type have been described in Berea sandstone by Menéndez et al. (1996) and in Darley Dale sandstone by Wu et al. (2000). The other instances of off-fault damage depict grain crushing where grains (or some portion of the grain) are broken into many pieces. Grain crushing is accompanied by the production of fine-grained debris and pore collapse (porosity reduction).

4. Discussion

4.1. Drainage Conditions Throughout Deformation

We deformed highly permeable porous sandstone samples at 3 different strain rates and observed the rate of fault propagation under different pore fluid pressures. All experiments were conducted at a constant differential pressure of 10 MPa. For samples deformed at the same strain rate, the peak stresses were similar regardless of the pore fluid pressure, in accordance with the effective stress law with $\alpha = 1$ (Table 2). In general, samples deformed at faster strain rates have higher peak stresses relative to samples deformed at slower strain rates (Figure 2; Table 2).

The post-failure behaviors vary depending on the strain rate used during the experiment. In samples deformed at 10^{-4} s^{-1}, similar faulting behaviors were observed irrespective of pore fluid pressures applied. When deformed at

a slower rate of 10^{-6} s^{-1}, samples exhibited slow faulting at high pore fluid pressures (>120 MPa). Microstructural analyses reveal pervasive grain crushing and pore collapse in samples failed by slow faulting (Figures 3–5). Slow faulting also results in broader fault zones and more off-fault damage (Figures 6 and 7).

In the traditional mechanical framework, dilatant hardening is expected to occur at sufficiently fast strain rates when the time scale for fluid diffusion is longer than the time scale for deformation (e.g., Brace & Martin, 1968; Duda & Renner, 2013). At fast strain rates, the rate of dilatant microcracking is faster and more likely to outpace the rate of fluid diffusion, which may lead to undrained deformation and dilatant hardening. At slow strain rates, the rate of dilatancy is slower and additional time is allowed for fluid diffusion, which may lead to drained deformation without dilatant hardening.

Following Duda and Renner (2013) and Fischer and Paterson (1992), we can estimate the diffusion time for water (t_f) in Darley Dale sandstone as follows:

$$t_f = L^2 * \eta * \frac{S}{k} \tag{1}$$

Using a viscosity of water (η) of 8.90×10^{-4} Pa.s. at 23°C (Korson et al., 1969), a storage capacity per unit volume (S) between 10^{-10} Pa^{-1} and 10^{-11} Pa^{-1} (Duda & Renner, 2013), a permeability (k) for Darley Dale between 10^{-13} m^2 and 10^{-14} m^2 (Zhu & Wong, 1997), and the half length of the sample ($L = 19.05$ mm), the estimated fluid diffusion time (t_f) ranges from 3×10^{-5} s to 3×10^{-3} s. The duration of brittle faulting, or the time elapsed between the sample reaching peak stress and the stress drop leveling off to residual stress, ranges from ~40 to ~9,000 s for an individual experiment (Figure 2). Using the duration of brittle faulting to approximate the timescale for deformation (t_d), we conclude that $t_f < t_d$, and deformation is drained at the sample scale during all experiments in this study. The described well-drained condition is consistent with other studies that demonstrate pore fluid pressure in Darley Dale sandstone readily equilibrates throughout the sample (e.g., Rutter & Hackston, 2017).

For all rocks deformed at a given strain rate, the elastic moduli during the quasi-elastic portion of loading were similar, and the peak stresses were also similar regardless of the magnitude of pore fluid pressure used in the experiment (Table 2). Little variation in peak stresses and Young's moduli in samples deformed at a given strain rate is further evidence for drained deformation proceeding in accordance with the effective stress law with $\alpha = 1$ (i.e., local variations in pore fluid pressure, if present, have negligible effect on deformation behaviors). Prior to peak stress, the deformation is accurately characterized by the value of the differential pressure ($P_{dif} = 10$ MPa) (e.g., Zimmerman et al., 1986).

After peak stress is attained, brittle faulting is dictated by crack growth and coalescence that initially occurs at much smaller length scales relative to the total sample length (e.g., Reches & Lockner, 1994). Prior to the formation of a macroscopic fault, localized crack growth and linkage results in local deformation rates that exceed the imposed macroscopic strain rate (e.g., Renard et al., 2019). Furthermore, the propagation of a fault in granular sandstones can result in permeability reduction despite volume increase of the sample because grain comminution in the fault zone is thought to generate more tortuous flow paths (Zhu & Wong, 1996).

Although estimating the drainage condition at small length scales is difficult, similar post-failure behaviors in all samples deformed at strain rates of 10^{-4} s^{-1} and 10^{-5} s^{-1} suggest drained conditions were maintained throughout fault growth at all pressure conditions. We did not measure local variations in pore fluid pressure during deformation as in other state-of-the-art studies (e.g., Aben & Brantut, 2021; Proctor et al., 2020). However, the results from experiments completed at fast strain rates suggest that local reductions in permeability and local increases in deformation rate, if any, did not cause dilatant hardening that was significant enough to affect faulting behavior (Figure 2). Since drained conditions are achieved in samples deformed at strain rates of 10^{-4} s^{-1} and 10^{-5} s^{-1}, samples deformed at 10^{-6} s^{-1} (larger t_d) can be considered fully drained. However, increasing pore fluid pressure had a significant effect on the post-failure behaviors and microstructures exclusively on samples deformed at 10^{-6} s^{-1}. Mechanisms other than dilatant hardening in the traditional sense must be responsible for the slow faulting at high pore fluid pressure under drained conditions.

4.2. Time-Independent versus Subcritical Crack Growth

Crack growth is often viewed as a time-independent, critical phenomenon where unstable crack growth occurs once a critical crack length or critical stress is attained (e.g., Griffith, 1921). However, subcritical crack growth is also known to play an important role in rock deformation (e.g., Atkinson, 1984; Heap et al., 2009). Fault growth

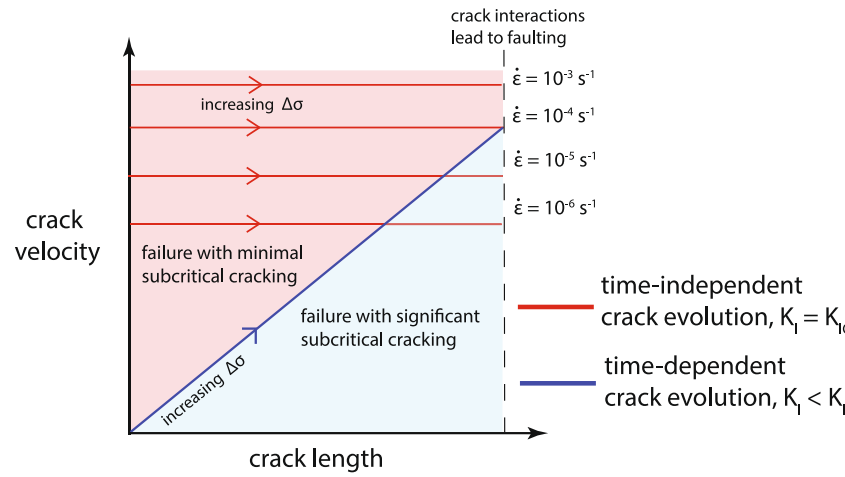

Figure 8. A schematic showing crack velocity versus crack length for both time-independent cracks growing by stress transfer and time-dependent cracks growing by stress corrosion. Cracks growing by stress transfer grow at a constant rate directly proportional to the imposed strain rate. Cracks growing by stress corrosion will grow progressively faster as additional differential stress is applied to the sample.

in rock under compression is known to be primarily controlled by the interaction and coalescence of tensile mode I cracks (Reches & Lockner, 1994). Without stress corrosion processes, time-independent crack growth occurs only if the intrinsic fracture toughness for mode I crack growth (K_{IC}) is achieved at the crack tip. For a mode I crack under compression, the mode I stress intensity factor (K_I) decreases as a function of crack length (i.e., crack growth is stable) (e.g., Brantut et al., 2012; Kachanov, 1982; Kemeny & Cook, 1991; Nemat-Nasser & Horii, 1982). Therefore, under compression, time-independent crack growth requires that additional stress is applied to the rock so the condition for crack growth (i.e., $K_I = K_{IC}$) continues to be met as the crack lengthens.

Constant stress creep tests are designed to deform a rock at a stress level below its time-independent failure strength. Under a constant stress, time-dependent brittle creep due to chemically assisted subcritical crack growth can be observed in water-saturated rocks (e.g., Heap et al., 2009). Due to brittle creep, maintaining a constant differential stress below the time-independent failure strength allows for the observed strain rate to change as a function of time. Under constant stress, a population of cracks will initially lengthen due to stress corrosion and result in a condition where $K_I < K_{IC}$ at the crack tips. The initial crack lengthening leads to a decrease in K_I at crack tips, a deceleration in crack velocities, and hence a deceleration in macroscopic strain rate (Brantut et al., 2012). A period of quasi-steady deformation occurs until crack interactions cause an increase K_I at crack tips and an increase in the macroscopic strain rate, which leads to brittle faulting even though the stress applied to the sample is constant (Brantut et al., 2012).

If the minimum rate of brittle creep observed during a constant stress test were to approach the strain rate used during a constant strain rate test, it would imply that the subcritical crack growth rate is similar to the rate of time-independent crack growth induced by stress transfer. When the subcritical crack growth rate approaches the constant strain rate, the sample can attain peak stress when the stress intensity factor at some number crack tips is less than the time-independent fracture toughness (i.e., $K_I < K_{IC}$) (Figure 8). Since subcritical cracks grow because of chemically assisted stress corrosion rather than by mechanically induced stress, fluid-saturated rocks deformed at slow strain rates fail at some level of stress below their theoretical time-independent failure strength. A reduction in rock strength with a reduction in strain rate occurs because the rate of subcritical crack growth can become significant when compared to the imposed deformation rate (e.g., Kemeny & Cook, 1991; Sano et al., 1981).

4.3. Influence of Subcritical Cracking on Shear Strength

To better examine creep data at a variety of differential pressures (i.e., $P_{dif} = P_c - P_f$), we plotted our data from the constant strain rate experiments and the brittle creep data extracted from Heap et al. (2009) and Brantut et al. (2013) in Figure 9. In this plot, the differential stress $\Delta\sigma$ is normalized (i.e., $\Delta\sigma_c / \Delta\sigma_{max}$), where $\Delta\sigma_{max}$ is the failure strength (peak stress) obtained in constant strain rate experiments. For the brittle creep data, $\Delta\sigma_{max}$ was

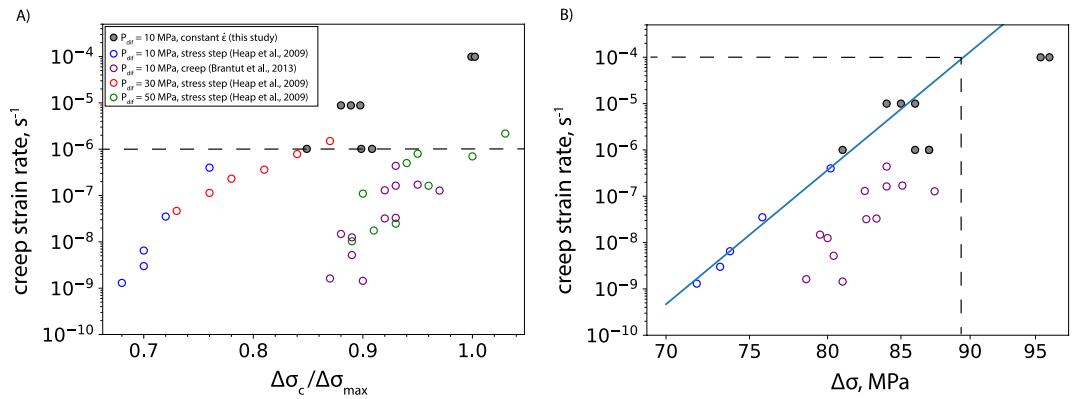

Figure 9. (a) Semi-log plot of creep strain rate versus creep stress ($\Delta\sigma_c$) divided by the peak differential stress ($\Delta\sigma_{max}$) observed in a compilation of constant stress creep experiments completed on Darley Dale sandstone (Heap 2009, Brantut et al., 2013). Data from this study (solid gray dots) were plotted using a $\Delta\sigma_{max}$ = 95 MPa. (b) Semi-log plot of creep strain rate versus differential stress ($\Delta\sigma$) from Heap et al. (2009) and Brantut et al. (2013).

extracted from Brantut et al. (2013) at a strain rate of 10^{-5} s^{-1}. For our data, $\Delta\sigma_{max}$ = 95 MPa, which was observed in experiments completed at 10^{-4} s^{-1} (Table 2; Figure 9a).

The decrease in peak stress with decreasing strain rate is best explained by weakening induced by subcritical crack growth because deformation is drained and dilatant hardening likely did not play a significant role, as previously discussed. Compared to samples deformed at a strain rate of 10^{-5} s^{-1}, the peak stresses observed at 10^{-4} s^{-1} are more representative of the time-independent strength of Darley Dale samples at P_{dif} = 10 MPa since the imposed deformation rate is much faster than the expected brittle creep rates (Figure 9a). At slower strain rates, brittle creep can be active in samples subjected to differential stress <95 MPa, regardless of whether the sample is deformed under a condition of constant stress or using a constant strain rate. Notably, the rate of brittle creep in Darley Dale can be at least 10^{-6} s^{-1} under a variety of conditions, and such creep strain rates recorded during creep tests are only representative of the minimum creep rate observed during secondary creep (Figure 9). Because the rate of brittle creep in Darley Dale is significant at levels well below the time-independent failure strength, the rate of brittle creep in the sample can exceed the slowest constant strain rate we have used in our experiments.

The dependence of creep strain rate on differential stress can be expressed as a power law

$$\dot{\varepsilon} = A(\Delta\sigma)^n \tag{2}$$

where A is a constant (Heap et al., 2009). Heap et al. (2009) reported a power law exponent (n) of 49.93. Using this value, we extrapolated the data from Heap et al. (2009) and Brantut et al. (2013) and determined that the expected creep strain rate is slower than 10^{-4} s^{-1} unless the differential stress exceeds ~89 MPa (Figure 9b). In other words, the rate of brittle creep is not comparable to the imposed strain rate of 10^{-4} s^{-1} until a minimum differential stress of 89 MPa is applied to the sample. Peak stress is generally higher at fast strain rates because the rate of subcritical crack growth is orders of magnitude lower than the strain rate for most of the experiment. The minimum rate of brittle creep only becomes comparable to the loading rate when the sample approaches the time-independent failure strength. By this time, most crack growth would have already occurred predominantly by stress transfer, and stress corrosion processes driving subcritical cracking growth would have little effect on peak stress (Figure 8). At 10^{-4} s^{-1}, there is simply not enough time for subcritical cracking to play an important role during deformation.

At lower loading rates of 10^{-5} s^{-1}and 10^{-6} s^{-1}, the rate of crack growth due to stress transfer is slower. When the expected minimum rate of brittle creep at a certain level of differential stress exceeds the constant loading rate, subcritical cracks due to stress corrosion would grow and accelerate during active loading. The resulting stress relaxation from the lengthening of subcritical cracks outpaces the rate at which additional stress is transferred to the crack tip via active loading. The reduction in peak stress suggests the rate of subcritical crack growth begins to exceed the rate of stress transfer at lower levels of differential stress when the strain rate is lowered from 10^{-4} s^{-1} to 10^{-6} s^{-1}. The reduction in peak stress as a function of the strain rate suggests that fault growth is increasingly

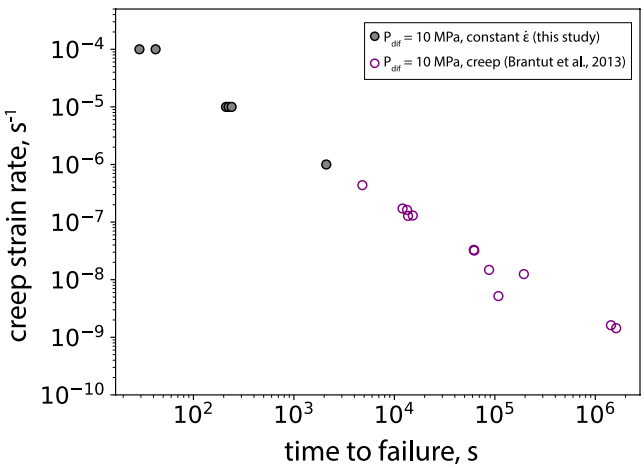

Figure 10. Creep strain rate plotted against time to failure on log-log axes for creep experiments from Brantut et al. (2013). For our experiments (solid dots), we plot the time elapsed between peak stress and the observed peak in slip velocity. Experiments where no acceleration in slip velocity could be discerned from the data are excluded from this plot.

dictated by subcritical as opposed to time-independent cracking at slow strain rates.

4.4. Strain Rate Dependent Time-to-Failure

Because the peak stresses in samples deformed at lower strain rates are below the time-independent failure strength, it is likely that the stress intensity at a significant portion of cracks tips remains below the time-independent fracture toughness ($K_I < K_{IC}$), even after peak stress is attained. We argue that when the strain rate is sufficiently low, faulting is increasingly controlled by the nucleation and coalescence of chemically-assisted subcritical cracks as opposed to the time-independent cracks resulting from stress transfer. Following this working hypothesis, the observed time lapse between the peak stress and spike in slip velocity can be explained by the competition between time-independent and subcritical cracking.

In constant strain rate experiments, the strain rate is inversely proportional to the elapsed time between the peak stress and measured acceleration in slip velocity (i.e., time-to-failure) (Figure 2i; Figure 10). At 10^{-4} s^{-1}, only a short time (<50 s) elapsed between peak stress and the observed peak in slip velocity. At 10^{-5} s^{-1} and 10^{-6} s^{-1}, a significantly longer time (~210 s–~2,100 s, respectively) elapsed between the peak stress and any detectable peak in slip velocity (Figure 2). In a creep test, time-to-failure is the time elapsed from when the sample is initially placed under constant stress to when the sample fails by brittle faulting and there is a rapid acceleration in strain rate (e.g., Brantut et al., 2013; Heap et al., 2009). Both the creep strain rate and constant strain rate scale similarly with time-to-failure: In both types of experiment, lower strain rates result in longer times-to-failure (Figure 10).

To better understand the relationship between time-to-failure and strain rate, consider a sample deformed at a very fast rate strain rate (e.g., $\geq 10^{-3}$ s^{-1}). Our data suggest time-to-failure would approach zero (Figure 10). Because time-to-failure in a constant strain rate experiment approaches zero at fast strain rates (Figure 10), time-independent deformation (i.e., $K_I = K_{IC}$) implies faulting occurs almost immediately after reaching peak differential stress. Now, recall that creep strain rate increases as a function of applied differential stress (Equation 2). A sample left to creep very close to its time-independent failure strength (i.e., $\Delta\sigma_c / \Delta\sigma_{max} \approx 1$) would have time-to-failure close to zero since time-to-failure decreases with an increase in creep strain rate (Figure 10). At high creep strain rates and high levels of differential stress, the time-to-failure is short primarily because subcritical crack growth commences at higher initial crack lengths. Higher initial crack lengths at higher differential stress imply less crack growth due stress corrosion is required before reaching the length at which crack interactions lead to failure. Relative to creep at low differential stress, creep initiated at a high level of differential stress results in less total cracking due stress corrosion, higher minimum creep strain rates, and shorter times to failure (Brantut et al., 2012).

The varying times-to-failure in our experiments can be explained by varying degrees of subcritical and time-independent crack growth that occurred after peak stress. At a strain rate of 10^{-4} s^{-1}, the effect of subcritical cracking on failure behavior is negligible compared to the stress transfer process (Figure 9; Figure 10b). At a strain rate of 10^{-6} s^{-1}, the rate of brittle creep approached the loading rate at lower levels of differential stress, and less total crack growth occurred through stress transfer (Figure 10). In samples deformed at a strain rate of 10^{-6} s^{-1}, times-to-failure are longer because crack growth and coalescence is dictated by stress corrosion processes as opposed to stress transfer due to active loading.

Times-to-failure observed at a strain rate of 10^{-5} s^{-1} represent an intermediate case where both stress transfer and subcritical cracking play a role. As expected, times-to-failure at a strain rate of 10^{-5} s^{-1} reflect less of a contribution from subcritical cracking than experiments at 10^{-6} s^{-1} but more significant subcritical cracking than those at 10^{-4} s^{-1}. Subcritical cracking causes the peak stress to be considerably lower than that at 10^{-4} s^{-1}, yet the strain rate is still sufficiently high so that the stress transfer dominates the failure process.

At a constant strain rate of 10^{-6} s^{-1} and $P_f = 2$ MPa, the observed time-to-failure is comparable to a sample deformed under a constant differential stress that experienced a creep strain rate of ~10^{-6} s^{-1} (Figure 10). The

similarity in expected times-to-failure in both types of experiments supports our working hypothesis that at this strain rate, subcritical crack growth and interaction exert controls over post-failure fault growth. Collectively, our observations support the idea that the slow faulting observed at slow strain rates is related to more prevalent chemically assisted, subcritical crack growth that occurs at a rate similar to or faster than the imposed deformation rate.

4.5. Mechanism of Slow Faulting Under Drained Conditions

We have adapted the framework of Brantut et al. (2012) to illustrate how subcritical crack growth affects brittle faulting during constant strain rate experiments. Since faulting in porous rocks occurs due to the interaction of many cracks of varying lengths (e.g., Lockner et al., 1992), it is appropriate to consider an "effective crack length" that characterizes the length of a network of interacting cracks. When the effective crack length reaches a certain value, overall crack interactions lead to faulting. Envisioning crack growth using an effective crack length is in accordance with our microstructural observations that show dense networks of cracks accompanied by grain crushing in the primary fault zone (e.g., Figures 3 and 4, 6–7).

We propose that at sufficiently slow strain rates, subcritical crack growth commenced at the onset of shear-induced dilatancy (*C'*) and controlled the inelastic and failure behaviors in porous rocks to various degrees. Time-independent crack growth occurs when $K_I = K_{IC}$ at the crack tips and proceeds at a constant velocity proportional to the imposed strain rate. At fast strain rates, time-independent cracking results in the continuous growth of flaws until an abrupt period of crack interaction leads to fast faulting at a high effective crack length (Figure 11, red line). At slow strain rates, cracking through stress transfer dominates until the expected rate of brittle creep approaches the loading rate (e.g., Figure 8). The transition from cracking occurring predominantly from stress transfer to stress corrosion occurs at peak stress. At peak stress, the rate of stress relaxation from subcritical cracking begins to outpace the rate of stress transfer from active loading. When differential stress begins to drop, the local stresses decrease around crack tips, and the rate of subcritical cracking decelerates. Eventually, the local stresses at the cracks increase once the networks of subcritical cracks reach an effective length where crack interactions dominate and lead to faulting (Figure 11, blue line).

At slow strain rates, crack interaction is expected to occur at shorter effective crack lengths than those at faster strain rates because lower peak stress is observed at slow strain rates (Brantut et al., 2012). Because slow faulting was observed under the conditions most conducive for subcritical cracking, our data indicate that the interaction of clusters of subcritical cracks were inhibited under high pore fluid pressures (Figure 11). Therefore, pervasive and distributed microcracking was observed in sampled deformed at high pore fluid pressures, which is the necessary condition for slow faulting under high pore fluid pressures.

In accordance with the conceptual model that we adopted from Brantut et al. (2012), rock failure under constant stress requires less mechanical work than actively deforming a sample to failure using a constant strain rate. Less work is required to break samples under constant stress because stress corrosion processes facilitate subcritical crack growth when $K_I < K_{IC}$ at the crack tip (Brantut et al., 2014). Equivalently, our samples that were deformed using a constant strain rate of 10^{-6} s^{-1} required less total mechanical work to break relative to samples deformed at 10^{-4} s^{-1} that exhibited higher peak stresses. Accordingly, enhanced subcritical cracking could be related to slower rates of faulting. At slow strain rates, less total mechanical energy is available in the system to rapidly propagate a fault because more diffuse cracking occurred due to stress corrosion. Our mechanical data support this interpretation because faulting is the fastest at 10^{-4} s^{-1}, slower at 10^{-5} s^{-1}, and the slowest at 10^{-6} s^{-1} when peak stresses are the lowest and the most subcritical cracking is expected (Figure 2). Furthermore, our microstructural analysis shows more pervasive microcracking and diffuse shear bands in samples deformed at slower strain rates and high pore fluid pressures, which suggests enhanced subcritical crack growth occurred under these conditions (e.g., Figures 3–7).

At slow strain rates, conditions of high pore fluid pressure may have various chemical and mechanical effects that make conditions for slow faulting more favorable. Chemically, conditions of high pore fluid pressure at slow strain rates may facilitate a more corrosive environment that results in the growth of more numerous subcritical cracks. High pore fluid pressure may change the chemical environment at the crack tip through some combination of increasing the autoionization of water and supplying more reactive species to the crack tip (Atkinson, 1984; Fyfe, 1978). However, determining to what extent increasing pore fluid pressure increases the rate of subcritical cracking requires a precise description of the chemical reactions responsible for chemical bond rupture. For

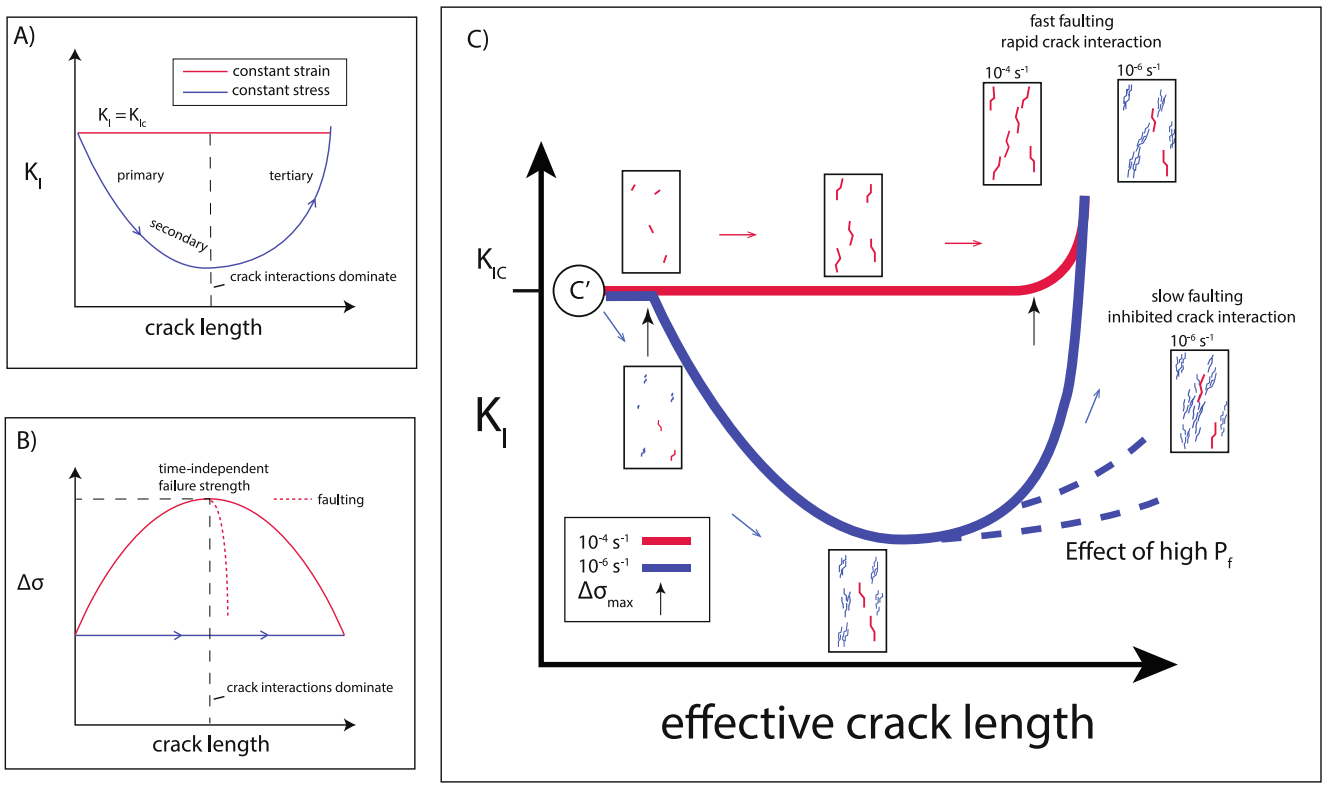

Figure 11. (a) Evolution of stress intensity factor and crack length for constant stress and constant strain rate experiments (adopted from Brantut et al., 2012). (b) Evolution of differential stress and crack length for both constant stress and constant strain rate experiments (adopted from Brantut et al., 2012). (c) Envisioned evolution of stress intensity factor and effective crack length for constant strain rate conditions used in this study. Blue dotted lines depict the stabilizing effect of high pore fluid pressure at slow strain rates.

example, some controversy exists as to whether molecular water (i.e., H_2O) or hydroxide (i.e., OH^-) from the ionization of water is the primary reactant driving stress corrosion (e.g., Atkinson, 1984; Atkinson & Meredith, 1981; Dove, 1995). Increasing pore fluid pressure increases the autoionization of water which increases the chemical activity of OH^-. Because the concentration of OH^- in solution is roughly an order of magnitude higher at $P_f = 180$ MPa relative to $P_f = 2$ MPa (Fyfe, 1978), reaction rate theory predicts a rate of reaction approximately an order of magnitude faster at $P_f = 180$ MPa relative to $P_f = 2$ MPa (e.g., Dove, 1995). However, an increase in the autoionization of water only matters if OH^- is a reactant participating in stress corrosion. It is also often argued that the rate of stress corrosion is diffusion-limited (e.g., Atkinson, 1984). If stress corrosion reactions are diffusion-limited and deformation is drained throughout the sample, it is possible that high P_f could serve as a mechanism for transporting more reactants, whether that be H_2O or OH^-, to new and lengthening crack tips. In this framework, any additional subcritical cracking facilitated by high P_f due to chemical effects may slow the rate of fault growth.

Mechanically, localized dilatant hardening enabled by pervasive subcritical cracking may have also hindered fault growth. Our microstructural analysis provides some evidence for locally undrained conditions caused by grain crushing and pore collapse in samples deformed at slow strain rates and high P_f. The observed differences in the microstructures presented in this study are important since the fracture network influences the permeability of the rock. When compared to the samples failed by abrupt faulting (Figure 3; Figure 5), the microstructures from samples failed by slow faulting were associated with higher crack densities (Figure 5), wider fault zones (Figure 6), and enhanced off-fault grain crushing (Figure 4; Figure 7). In dilating porous rock, grain crushing induced by intense microcracking can lead to increasingly tortuous flow paths and permeability reduction (Zhu & Wong, 1996). Although deformation is drained at the sample length scale, we cannot rule out the possibility of locally undrained pockets forming in our samples.

Notably, there is a considerable amount of clay present in Darley Dale sandstone (~5%) (Heap et al., 2009). The permeability of aggregates of clay minerals may range from 10^{-19} m^2 to 10^{-24} m^2, which is much lower

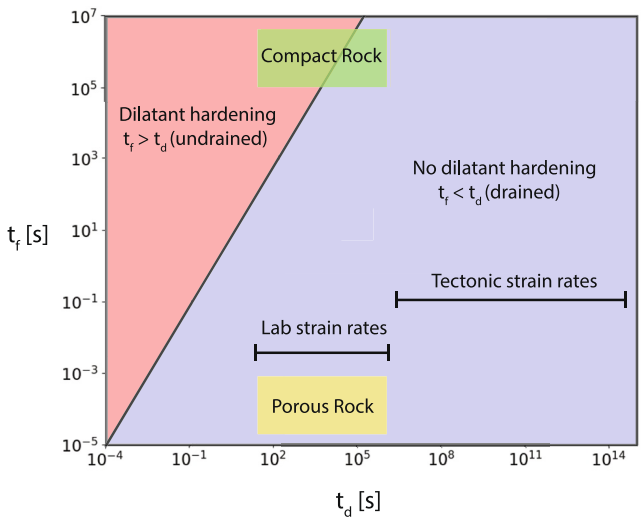

Figure 12. t_f and t_d are plotted for typical geomaterials and strain rates as labeled. Definitions for deformation and diffusion timescales follow Fischer and Paterson (1992). Red shaded area highlights conditions for undrained deformation which facilitates dilatant hardening. Blue shaded area highlights conditions for drained deformation where dilatant hardening cannot occur.

than the bulk permeability of Darley Dale sandstone ($\sim 10^{-13}$ m^2) (Behnsen & Faulkner, 2011). Additionally, our microstructural analysis supports the notion that pervasive subcritical cracking enabled grain crushing and pore collapse, which would cause local permeability reduction. Low-permeability patches present around clay minerals and crushed grains may have generated local permeability reduction significant enough to affect fluid flow into and out of the subcritical cracks. In addition to the chemical effects of high pore fluid pressure on subcritical cracking, it is conceivable that localized dilatant hardening can impede the growth and coalescence of subcritical cracks that contribute to slow faulting under drained conditions at high P_f. Finally, the previously mentioned chemical and mechanical mechanisms may co-exist, and slow faulting may also be controlled by a coupled chemo-mechanical processes. Further work is required to discern which processes exert the most important controls over fault growth.

4.6. Implications for Natural Fault Growth

Our experimental data on porous sandstone samples show that high pore fluid pressure can stabilize fault propagation during drained deformation in porous rocks only under slow strain rates. This is apparently contradicting conventional wisdom that dilatant hardening is more prevalent at fast deformation rates where undrained conditions are present. We propose that slow faulting at slow strain rates results from the interplay between dilatant hardening and subcritical crack growth occurring at conditions of high pore fluid pressures due to chemical effects. Our microstructural analysis of samples that failed by slow faulting suggests that grain crushing may have led to locally undrained conditions conducive to dilatant hardening. Our results suggest that the effect of dilatant hardening on subcritical crack growth may not be highly sensitive to lithology and the bulk hydraulic properties of the sample; instead, local variations in permeability may likely have a large control over the eventual faulting behavior. This observation has important implications in tectonic fault growth where stress corrosion cracking is prevalent and drained conditions are maintained (e.g., Zoback & Townend, 2001) due to very slow strain rates (Figure 12).

For instance, tidally induced tremor activities are observed along the San Andreas fault (Thomas et al., 2009). Becken et al. (2011) show that these tremor actives coincide with a large, low-resistivity area located in the lower-crust and upper mantle beneath Parkfield that is often interpreted as a fluid source. The migration of mantle-derived fluid from permeable zones of low-resistivity to more impermeable regions of the fault is thought to modulate the occurrence of non-volcanic tremor at conditions of high pore fluid pressure (Becken et al., 2011). Our experimental observations of slow faulting under drained conditions provide an alternative explanation of these slow slip events. The interplay between dilatant hardening and subcritical crack growth at conditions of high pore fluid pressure should be further explored since subcritical crack growth and brittle creep dominate fault growth in Earth's upper crust.

Along natural faults, the stabilizing effect of dilatant hardening is thought to be mediated by thermal weakening mechanisms that occur during fault slip such as flash heating and thermal pressurization (e.g., Segall et al., 2010; Brantut, 2021). Rice (2006) has shown that the most significant perturbations in temperature and pore fluid pressures during fault rupture occur tens of millimeters from the principal slip surface of a given fault. However, the permeability of rocks located in close proximity (<100 mm) to the principal slip surface of a fault may vary by up to five orders of magnitude (e.g., Wibberley & Shimamoto, 2003). Clearly, determining the drainage condition from the bulk hydraulic properties of a large rock sample does not capture the variation in hydraulic properties that are present at much smaller length scales. In both a laboratory setting and along natural faults, localized, small-scale permeability heterogeneities have the potential to affect how quickly fluid eventually flows into newly created void spaces. Therefore, it is possible for dilatant hardening to manifest over both large and small length scales depending on the permeability structure of a given rock. Because of the structural complexity of natural faults, the evolution of permeability and pore fluid pressure throughout the seismic cycle is complicated. This study also highlights the need to explore permeability evolution of rocks deformed at a wide range of strain rates and pore fluid pressures to better understand slow faulting.

5. Concluding Remarks

We have demonstrated that varying time-independent and subcritical cracking by changing the strain rate can result in different faulting behaviors. Additionally, we showed that conditions of high pore fluid pressure can stabilize faulting in samples deformed under drained conditions. We examined the interplay between time-dependent and time-independent cracking and show that subcritical crack growth can affect both the shear strength and the post-failure fault growth in samples deformed at a sufficiently low strain rate.

For Darley Dale sandstone, we demonstrated that the rate of brittle creep can exceed 10^{-6} s^{-1} at levels below the time-independent failure strength. Based on our mechanical and microstructural analysis, we postulated that at 10^{-6} s^{-1}, subcritical crack growth in addition to crack growth via stress transfer controls the inelastic and failure behaviors. We propose that the observed stabilization effect of high pore pressure at the lowest strain rate was due to a combination of enhanced subcritical crack growth and dilatant hardening impeding such cracking at the grain scale. The proposed mechanism slow faulting may have important implications for natural fault growth.

Conflict of Interest

The authors declare no conflicts of interest relevant to this study.

Data Availability Statement

Mechanical data used to make Figure 2 and Figure S1 in Supporting Information S1 and photomicrographs are in an open science framework (OSF) database (Zega & Zhu, 2023).

Acknowledgments
This research is supported by the USGS National Earthquake Hazard Reduction Program (NEHRP) under Grant G22AP00036 and the National Science Foundation under Grant EAR-2218314. We thank Dr. N. Brantut for furnishing us with the Darley Dale sandstone. We thank Dr. T. Kanaya for his assistance on the initial experimental setup and discussion. We also thank Dr. P. Piccoli and Dr. S. Penniston-Dorland for their help using the microscope.

References

Aben, F. M., & Brantut, N. (2021). Dilatancy stabilises shear failure in rock. *Earth and Planetary Science Letters*, *574*, 117174. https://doi.org/10.1016/j.epsl.2021.117174

Anderson, O. L., & Grew, P. C. (1977). Stress corrosion theory of crack propagation with applications to geophysics. *Reviews of Geophysics*, *15*(1), 77–104. https://doi.org/10.1029/RG015i001p00077

Atkinson, B. K. (1984). Subcritical crack growth in geological materials. *Journal of Geophysical Research*, *89*(B6), 4077–4114. https://doi.org/10.1029/JB089iB06p04077

Atkinson, B. K., & Meredith, P. G. (1981). Stress corrosion cracking of quartz: A note on the influence of chemical environment. *Tectonophysics*, *77*(1), T1–T11. https://doi.org/10.1016/0040-1951(81)90157-8

Baud, P., Zhu, W., & Wong, T. (2000). Failure mode and weakening effect of water on sandstone. *Journal of Geophysical Research*, *105*(B7), 16371–16389. https://doi.org/10.1029/2000JB900087

Becken, M., Ritter, O., Bedrosian, P. A., & Weckmann, U. (2011). Correlation between deep fluids, tremor and creep along the central San Andreas fault. *Nature*, *480*(7375), 87–90. Article 7375. https://doi.org/10.1038/nature10609

Bedford, J. D., Faulkner, D. R., Allen, M. J., & Hirose, T. (2021). The stabilizing effect of high pore-fluid pressure along subduction megathrust faults: Evidence from friction experiments on accretionary sediments from the Nankai Trough. *Earth and Planetary Science Letters*, *574*, 117161. https://doi.org/10.1016/j.epsl.2021.117161

Behnsen, J., & Faulkner, D. R. (2011). Water and argon permeability of phyllosilicate powders under medium to high pressure. *Journal of Geophysical Research*, *116*(B12), B12203. https://doi.org/10.1029/2011JB008600

Bernabe, Y., & Brace, W. F. (1990). Deformation and fracture of Berea sandstone. In *The brittle-Ductile transition in rocks* (pp. 91–101). American Geophysical Union (AGU). https://doi.org/10.1029/GM056p0091

Brace, W. F., & Martin, R. J. (1968). A test of the law of effective stress for crystalline rocks of low porosity. *International Journal of Rock Mechanics and Mining Sciences & Geomechanics Abstracts*, *5*(5), 415–426. https://doi.org/10.1016/0148-9062(68)90045-4

Brace, W. F., Paulding, B. W., & Scholz, C. (1966). Dilatancy in the fracture of crystalline rocks. *Journal of Geophysical Research*, *71*(16), 3939–3953. https://doi.org/10.1029/JZ071i016p03939

Brantut, N. (2021). Dilatancy toughening of shear cracks and implications for slow rupture propagation. *Journal of Geophysical Research: Solid Earth*, *126*(11), e2021JB022239. https://doi.org/10.1029/2021JB022239

Brantut, N., Baud, P., Heap, M. J., & Meredith, P. G. (2012). Micromechanics of brittle creep in rocks. *Journal of Geophysical Research*, *117*(B8), a–n. https://doi.org/10.1029/2012JB009299

Brantut, N., Heap, M. J., Baud, P., & Meredith, P. G. (2014). Rate- and strain-dependent brittle deformation of rocks. *Journal of Geophysical Research: Solid Earth*, *119*(3), 1818–1836. https://doi.org/10.1002/2013JB010448

Brantut, N., Heap, M. J., Meredith, P. G., & Baud, P. (2013). Time-dependent cracking and brittle creep in crustal rocks: A review. *Journal of Structural Geology*, *52*, 17–43. https://doi.org/10.1016/j.jsg.2013.03.007

Dal Zilio, L., Lapusta, N., & Avouac, J.-P. (2020). Unraveling scaling properties of slow-slip events. *Geophysical Research Letters*, *47*(10), e2020GL087477. https://doi.org/10.1029/2020GL087477

Dove, P. M. (1995). Geochemical controls on the kinetics of quartz fracture at subcritical tensile stresses. *Journal of Geophysical Research*, *100*(B11), 22349–22359. https://doi.org/10.1029/95JB02155

Duda, M., & Renner, J. (2013). The weakening effect of water on the brittle failure strength of sandstone. *Geophysical Journal International*, *192*(3), 1091–1108. https://doi.org/10.1093/gji/ggs090

Fischer, G. J., & Paterson, M. S. (1992). Chapter 9 measurement of permeability and storage capacity in rocks during deformation at high temperature and pressure. In B. Evans & T. Wong (Eds.), *International geophysics* (Vol. 51, pp. 213–252). Academic Press. https://doi.org/10.1016/S0074-6142(08)62824-7

French, M. E., & Zhu, W. (2017). Slow fault propagation in serpentinite under conditions of high pore fluid pressure. *Earth and Planetary Science Letters*, *473*, 131–140. https://doi.org/10.1016/j.epsl.2017.06.009

Fyfe, W. S. (1978). *Fluids in the earth's crust: Their significance in metamorphic, tectonic and chemical transport process*. Elsevier.

Griffith, A. A. (1921). VI. The phenomena of rupture and flow in solids. *Philosophical Transactions of the Royal Society of London - Series A: Containing Papers of a Mathematical or Physical Character*, *221*(582–593), 163–198. https://doi.org/10.1098/rsta.1921.0006

Hadizadeh, J., & Law, R. D. (1991). Water-weakening of sandstone and quartzite deformed at various stress and strain rates. *International Journal of Rock Mechanics and Mining Sciences & Geomechanics Abstracts*, *28*(5), 431–439. https://doi.org/10.1016/0148-9062(91)90081-V

Heap, M. J., Baud, P., Meredith, P. G., Bell, A. F., & Main, I. G. (2009). Time-dependent brittle creep in Darley Dale sandstone. *Journal of Geophysical Research*, *114*(B7), B07203. https://doi.org/10.1029/2008JB006212

Kachanov, M. L. (1982). Microcrack model of rock inelasticity part III: Time-dependent growth of microcracks. *Mechanics of Materials*, *1*(2), 123–129. https://doi.org/10.1016/0167-6636(82)90040-0

Kemeny, J. M., & Cook, N. G. W. (1991). Micromechanics of deformation in rocks. In S. P. Shah (Ed.), *Toughening mechanisms in quasi-brittle materials* (pp. 155–188). Springer Netherlands. https://doi.org/10.1007/978-94-011-3388-3_10

Korson, L., Drost-Hansen, W., & Millero, F. J. (1969). Viscosity of water at various temperatures. *The Journal of Physical Chemistry*, *73*(1), 34–39. https://doi.org/10.1021/j100721a006

Liu, Y., & Rice, J. R. (2007). Spontaneous and triggered aseismic deformation transients in a subduction fault model. *Journal of Geophysical Research*, *112*(B9), B09404. https://doi.org/10.1029/2007JB004930

Lockner, D. A., & Byerlee, J. D. (1994). Dilatancy in hydraulically isolated faults and the suppression of instability. *Geophysical Research Letters*, *21*(22), 2353–2356. https://doi.org/10.1029/94GL02366

Lockner, D. A., Byerlee, J. D., Kuksenko, V., Ponomarev, A., & Sidorin, A. (1992). Observations of quasistatic fault growth from acoustic emissions. In B. Evans & T. Wong (Eds.), *International geophysics* (Vol. 51, pp. 3–31). Academic Press. https://doi.org/10.1016/S0074-6142(08)62813-2

Martin, R. J. (1980). Pore pressure stabilization of failure in westerly granite. *Geophysical Research Letters*, *7*(5), 404–406. https://doi.org/10.1029/GL007i005p00404

Martin, R. J., III, & Durham, W. B. (1975). Mechanisms of crack growth in quartz. *Journal of Geophysical Research*, *80*(35), 4837–4844. https://doi.org/10.1029/JB080i035p04837

Menéndez, B., Zhu, W., & Wong, T.-F. (1996). Micromechanics of brittle faulting and cataclastic flow in Berea sandstone. *Journal of Structural Geology*, *18*(1), 1–16. https://doi.org/10.1016/0191-8141(95)00076-P

Nemat-Nasser, S., & Horii, H. (1982). Compression-induced nonplanar crack extension with application to splitting, exfoliation, and rockburst. *Journal of Geophysical Research*, *87*(B8), 6805–6821. https://doi.org/10.1029/JB087iB08p06805

Obara, K. (2002). Nonvolcanic deep tremor associated with subduction in southwest Japan. *Science*, *296*(5573), 1679–1681. https://doi.org/10.1126/science.1070378

Ougier-Simonin, A., & Zhu, W. (2015). Effect of pore pressure buildup on slowness of rupture propagation. *Journal of Geophysical Research: Solid Earth*, *120*(12), 7966–7985. https://doi.org/10.1002/2015JB012047

Paterson, M. S. & Wong, T. (Eds.) (2005). The role of pore fluids, *Experimental rock deformation—the brittle Field* (pp. 147–163). Springer. https://doi.org/10.1007/3-540-26339-X_7

Peng, Z., & Gomberg, J. (2010). An integrated perspective of the continuum between earthquakes and slow-slip phenomena. *Nature Geoscience*, *3*(9), 599–607. https://doi.org/10.1038/ngeo940

Proctor, B., Lockner, D. A., Kilgore, B. D., Mitchell, T. M., & Beeler, N. M. (2020). Direct evidence for fluid pressure, dilatancy, and compaction affecting slip in isolated faults. *Geophysical Research Letters*, *47*(16), e2019GL086767. https://doi.org/10.1029/2019GL086767

Reches, Z., & Lockner, D. A. (1994). Nucleation and growth of faults in brittle rocks. *Journal of Geophysical Research*, *99*(B9), 18159–18173. https://doi.org/10.1029/94JB00115

Renard, F., McBeck, J., Cordonnier, B., Zheng, X., Kandula, N., Sanchez, J. R., et al. (2019). Dynamic in situ three-dimensional imaging and digital volume correlation analysis to quantify strain localization and fracture coalescence in sandstone. *Pure and Applied Geophysics*, *176*(3), 1083–1115. https://doi.org/10.1007/s00024-018-2003-x

Rice, J. R. (1975). On the stability of dilatant hardening for saturated rock masses. *Journal of Geophysical Research*, *80*(11), 1531–1536. https://doi.org/10.1029/JB080i011p01531

Rice, J. R. (2006). Heating and weakening of faults during earthquake slip. *Journal of Geophysical Research*, *111*(B5). https://doi.org/10.1029/2005JB004006

Rice, J. R., & Rudnicki, J. W. (1979). Earthquake precursory effects due to pore fluid stabilization of a weakening fault zone. *Journal of Geophysical Research*, *84*(B5), 2177–2193. https://doi.org/10.1029/JB084iB05p02177

Rudnicki, J. W., & Chen, C.-H. (1988). Stabilization of rapid frictional slip on a weakening fault by dilatant hardening. *Journal of Geophysical Research*, *93*(B5), 4745–4757. https://doi.org/10.1029/JB093iB05p04745

Rudnicki, J. W., & Zhan, Y. (2020). Effect of pressure rate on rate and state frictional slip. *Geophysical Research Letters*, *47*(21), e2020GL089426. https://doi.org/10.1029/2020GL089426

Rutter, E., & Hackston, A. (2017). On the effective stress law for rock-on-rock frictional sliding, and fault slip triggered by means of fluid injection. *Philosophical Transactions of the Royal Society A: Mathematical, Physical & Engineering Sciences*, *375*(2103), 20160001. https://doi.org/10.1098/rsta.2016.0001

Sano, O., Ito, I., & Terada, M. (1981). Influence of strain rate on dilatancy and strength of Oshima granite under uniaxial compression. *Journal of Geophysical Research*, *86*(B10), 9299–9311. https://doi.org/10.1029/JB086iB10p09299

Scholz, C. (2002). The mechanics of earthquake faulting. https://doi.org/10.1017/CBO9780511818516

Scholz, C. H. (1972). Static fatigue of quartz. *Journal of Geophysical Research*, *77*(11), 2104–2114. https://doi.org/10.1029/JB077i011p02104

Segall, P., Rubin, A. M., Bradley, A. M., & Rice, J. R. (2010). Dilatant strengthening as a mechanism for slow slip events. *Journal of Geophysical Research*, *115*(B12), B12305. https://doi.org/10.1029/2010JB007449

Shelly, D. R., Beroza, G. C., Ide, S., & Nakamula, S. (2006). Low-frequency earthquakes in Shikoku, Japan, and their relationship to episodic tremor and slip. *Nature*, *442*(7099), 188–191. https://doi.org/10.1038/nature04931

Tamarkin, T., Ougier-Simonin, A., & Zhu, W. (2012). Progressive microscopic damage associated with fault growth. *Geophysical Research Letters*, *39*(15). https://doi.org/10.1029/2012GL052487

Terzaghi, K. (1943). *Theoretical soil mechanics*. John Wiley & Sons, Inc. https://doi.org/10.1002/9780470172766

Thomas, A. M., Nadeau, R. M., & Bürgmann, R. (2009). Tremor-tide correlations and near-lithostatic pore pressure on the deep San Andreas fault. *Nature*, *462*(7276), 1048–1051. Article 7276. https://doi.org/10.1038/nature08654

Underwood, E. E. (1969). Stereology, or the quantitative evaluation of microstructures. *Journal of Microscopy*, *89*(2), 161–180. https://doi.org/10.1111/j.1365-2818.1969.tb00663.x

Wibberley, C. A. J., & Shimamoto, T. (2003). Internal structure and permeability of major strike-slip fault zones: The median tectonic line in Mie Prefecture, Southwest Japan. *Journal of Structural Geology*, *25*(1), 59–78. https://doi.org/10.1016/S0191-8141(02)00014-7

Wong, T., David, C., & Zhu, W. (1997). The transition from brittle faulting to cataclastic flow in porous sandstones: Mechanical deformation. *Journal of Geophysical Research*, *102*(B2), 3009–3025. https://doi.org/10.1029/96JB03281

Wu, X. Y., Baud, P., & Wong, T. (2000). Micromechanics of compressive failure and spatial evolution of anisotropic damage in Darley Dale sandstone. *International Journal of Rock Mechanics and Mining Sciences*, *37*(1), 143–160. https://doi.org/10.1016/S1365-1609(99)00093-3

Xing, T., Zhu, W., French, M., & Belzer, B. (2019). Stabilizing effect of high pore fluid pressure on slip behaviors of gouge-bearing faults. *Journal of Geophysical Research: Solid Earth*, *124*(9), 9526–9545. https://doi.org/10.1029/2019JB018002

Zega, Z. J., & Zhu, W. (2023). Investigation of faulting behaviors at high pore fluid pressure. Dataset. https://doi.org/10.17605/OSF.IO/45EWA

Zhang, J., Wong, T.-F., & Davis, D. M. (1990). Micromechanics of pressure-induced grain crushing in porous rocks. *Journal of Geophysical Research*, *95*(B1), 341–352. https://doi.org/10.1029/JB095iB01p00341

Zhu, W., & Wong, T. (1997). The transition from brittle faulting to cataclastic flow: Permeability evolution. *Journal of Geophysical Research*, *102*(B2), 3027–3041. https://doi.org/10.1029/96JB03282

Zhu, W., & Wong, T.-F. (1996). Permeability reduction in a dilating rock: Network modeling of damage and tortuosity. *Geophysical Research Letters*, *23*(22), 3099–3102. https://doi.org/10.1029/96GL03078

Zimmerman, R. W., Somerton, W. H., & King, M. S. (1986). Compressibility of porous rocks. *Journal of Geophysical Research*, *91*(B12), 12765–12777. https://doi.org/10.1029/JB091iB12p12765

Zoback, M. D., & Townend, J. (2001). Implications of hydrostatic pore pressures and high crustal strength for the deformation of intraplate lithosphere. *Tectonophysics*, *336*(1), 19–30. https://doi.org/10.1016/S0040-1951(01)00091-9